©2024 Society of Economic Geologists, Inc.
Economic Geology, v. XXX, no. XX, pp. X–X

SCIENTIFIC COMMUNICATIONS

ORIGIN OF VOLCANIC-HOSTED MAGNETITE AT THE LAGUNA DEL MAULE COMPLEX, CHILE: A NEW EXAMPLE OF ANDEAN IRON OXIDE-APATITE MINERALIZATION

Ernesto Cofré,[1,†] Martin Reich,[1,2] J. Tomás Ovalle,[1,3,4] Gisella Palma,[1,3]
Fernando Barra,[1,2] Artur Deditius,[5,6] Adam C. Simon,[4] Malcolm Roberts,[7] and Brian R. Jicha[8]

[1] *Department of Geology and Millennium Nucleus for Metal Tracing Along Subduction, Faculty of Physical Sciences and Mathematics (FCFM), Universidad de Chile, Santiago, Plaza Ercilla 803, Chile*

[2] *Andean Geothermal Center of Excellence (CEGA), Faculty of Physical Sciences and Mathematics (FCFM), Universidad de Chile, Santiago, Plaza Ercilla 803, Chile*

[3] *School of Geology, Universidad Mayor, Av. Manuel Montt 367, Santiago, Chile*

[4] *Department of Earth and Environmental Sciences, University of Michigan, 1100 North University Avenue, Ann Arbor, Michigan 48109-1005*

[5] *Discipline of Mathematics, Statistics, Chemistry and Physics, Murdoch University, Murdoch, Western Australia 6150, Australia*

[6] *School of Earth Sciences, The University of Western Australia, Perth, Western Australia 6009, Australia*

[7] *Centre for Microscopy, Characterization and Analysis (CMCA), The University of Western Australia, Perth, Western Australia 6009, Australia*

[8] *Department of Geoscience, University of Wisconsin-Madison, 1215 West Dayton Street, Madison, Wisconsin 53706*

Abstract

Iron oxide-apatite (IOA) deposits, also known as magnetite-apatite or Kiruna-type deposits, are a major source of iron and potentially of rare earth elements and phosphorus. To date, the youngest representative of this group is the Pleistocene (~2 Ma) El Laco deposit, located in the Andean Cordillera of northern Chile. El Laco is considered a unique type of IOA deposit because of its young age and its volcanic-like features. Here we report the occurrence of similarly young IOA-type mineralization hosted within the Laguna del Maule Volcanic Complex, an unusually large and recent silicic volcanic system in the south-central Andes. We combined field observations and aerial drone images with detailed petrographic observations, electron microprobe analysis (EMPA), and ^{40}Ar/^{39}Ar dating to characterize the magnetite mineralization—named here "Vetas del Maule"—hosted within andesites of the now extinct La Zorra volcano (^{40}Ar/^{39}Ar plateau age of 1.013 ± 0.028 Ma). Five different styles of magnetite mineralization were identified: (1) massive magnetite, (2) pyroxene-actinolite-magnetite veins, (3) magnetite hydrothermal breccias, (4) disseminated magnetite, and (5) pyroxene-actinolite veins with minor magnetite. Field observations and aerial drone imaging, coupled with microtextural and microanalytical data, suggest a predominantly hydrothermal origin for the different types of mineralization. ^{40}Ar/^{39}Ar incremental heating of phlogopite associated with the magnetite mineralization yielded a plateau age of 873.6 ± 30.3 ka, confirming that the emplacement of Vetas del Maule postdated that of the host andesite rocks. Our data support the hypothesis that the magnetite mineralization formed in a volcanic setting from Fe-rich fluids exsolved from a magma at depth. Ultimately, Vetas del Maule provides evidence that volcanic-related IOA mineralization may be more common than previously thought, opening new opportunities of research and exploration for this ore deposit type in active volcanic arcs.

Introduction

Iron oxide-apatite (IOA) deposits represent the Cu-poor end member of the iron oxide copper-gold (IOCG) clan (Sillitoe, 2003; Barton, 2014). They are a major source of iron and potentially of rare earth elements and phosphorus (Mumin et al., 2007; Barton, 2014; Taylor et al., 2019). IOA mineralization is dominated by magnetite, which can be accompanied by variable amounts (1–50% modal) of apatite, actinolite, pyroxene, epidote, and Fe-(Cu) sulfides (Williams et al., 2005; Reich et al., 2022). IOA deposits occur globally with reported ages ranging from Proterozoic (Kiruna and Grängesberg districts, Sweden, and Pea Ridge and Pilot Knob, Missouri), Paleozoic (Bafq district, Iran), Cretaceous (Chilean iron belt), and Oligocene to Pleistocene (Cerro de Mercado, Mexico, and El Laco, Chile) (Nyström and Henríquez, 1994; Jonsson et al., 2013; Childress et al., 2016; Day et al., 2016; Heidarian et al., 2016; Westhues et al., 2017a, b; Corona-Esquivel et al., 2018; Ovalle et al., 2018; Simon et al., 2018; Peters et al., 2019; Troll et al., 2019; Reich et al., 2022).

The origin of IOA deposits remains debated, and several hypotheses have been proposed over the years to explain their formation. Liquid immiscibility models propose that massive magnetite orebodies are formed by emplacement of hydrous Fe-Ca-P melts or molten salts separated from silicate magmas (Nyström and Henríquez, 1994; Naslund et al., 2002; Tornos et al., 2016, 2024; Velasco et al., 2016; Hou et al., 2018; Mun-

---

[†] Corresponding author: e-mail, ercofrea@gmail.com

ISSN 0361-0128; doi:10.5382/econgeo.5093; 20 p.

Submitted: October 27, 2022 / Accepted: March 29, 2024

Digital appendices are available in the online Supplements section.

gall et al., 2018; Bain et al., 2020, 2021; Keller et al., 2022). Other authors have favored models that involve magnetite precipitation from Fe-rich and hypersaline magmatic-hydrothermal fluids sourced from subvolcanic intrusions (Hitzman et al., 1992; Rhodes and Oreskes, 1999; Sillitoe and Burrows, 2002; Barton and Johnson, 2004; Barton, 2014; Dare et al., 2015; Knipping et al., 2015a, b; Ovalle et al., 2018, 2022; Simon et al., 2018; Zhao et al., 2024). Regardless of the specific ore-forming mechanisms, all formation models invoke processes operating in an upper crustal environment, typically in extensional settings within a subduction context (Reich et al., 2022).

During the last decade, several studies have focused on IOA deposits located within the Coastal Cordillera and the Andes of northern Chile (Simon et al., 2018; Reich et al., 2022, and references therein). Palma et al. (2020, 2021) concluded that IOA deposits within this province can be classified into subtypes based on their geologic occurrence, mineralogical/geochemical features, and formation conditions. IOA subtypes range from deep magmatic-hydrothermal deposits (Los Colorados) to more transitional examples where hydrothermal signatures are dominant (e.g., El Romeral and Cerro Negro Norte). Pegmatitic-like, apatite-rich (>40% modal) systems, such as the Carmen, Fresia, and Mariela deposits and the subvolcanic/aerial deposit of El Laco, would represent shallow examples of this deposit class (Ovalle et al., 2018; Palma et al., 2019, 2020, 2021; Childress et al., 2020; La Cruz et al., 2020). The youngest IOA deposit reported so far is El Laco (~2 Ma), located in the Altiplano-Puna region of the Chilean Andes. El Laco is apparently a unique case because of its volcanic features resembling magnetite lava flows and because of its location within the Andean Cordillera (Nyström and Henriquez, 1994; Sillitoe and Burrows, 2002; Naranjo et al., 2010; Tornos et al., 2016, 2024; Velasco et al., 2016; Ovalle et al., 2018, 2022, 2023).

In this study, we report the occurrence of a <1.0 Ma IOA-type mineralization—named here Vetas del Maule (translated "Veins of Maule")—hosted within the Laguna del Maule Volcanic Complex in the Andes of south-central Chile (35°59′S, 70°25′30″W) (Fig. 1). The Laguna del Maule Volcanic Complex encompasses an area of 500 km^2 around a 15- × 20-km volcanic caldera, whose formation marks the beginning of volcanic activity around 1.5 m.y. ago (Hildreth et al., 2010). Intense volcanism has occurred since then, with an estimate of at least 50 eruptions and the formation of dozens of lava domes (Hildreth et al., 2010; Andersen et al., 2017). The Vetas del Maule magnetite mineralization is hosted within andesitic lavas of the La Zorra volcano, which has been dated at 1.013 ± 0.028 Ma (^{40}Ar/^{39}Ar plateau age, Hildreth et al., 2010). As such, this occurrence provides the opportunity to investigate one of the world's youngest examples of IOA-type mineralization in an active volcanic arc. Here we aim to document the occurrence of IOA-type mineralization in this segment of the Andean Cordillera and unravel the geologic and physicochemical conditions of magnetite formation. To achieve this goal, we carried out field observations and aerial drone imaging, followed by a detailed petrographic characterization of the different magnetite occurrences using polarized-light microscopy and scanning electron microscopy (SEM). In addition, we performed electron microprobe analyses (EMPA) and collected wavelength-dispersive spectrometry (WDS) elemental maps of magnetite. These data were used to characterize each magnetite type and to obtain information about formation conditions. Finally, we constrained the age of magnetite mineralization by means of ^{40}Ar/^{39}Ar dating of paragenetically related phlogopite. The new data are used to propose a genetic model for the Vetas del Maule magnetite mineralization, which highlights the link between volcanic processes and iron mineralization in active arcs.

Geologic Setting

The Laguna del Maule Volcanic Complex is located within the Transitional Southern volcanic zone in south-central Chile (34°30'–37°S) (Fig. 1A). The geotectonic configuration is defined by a dextral-oblique convergence between the South American and Nazca plates, with a convergence rate of 7 to 9 cm/yr that has been relatively constant during the last 20 m.y. (Pardo-Casas and Molnar, 1987; Hildreth and Moorbath, 1988). The Transitional Southern volcanic zone is characterized by an average crustal thickness of ~35 to 40 km, reaching up to 40 to 50 km below the Laguna del Maule Volcanic Complex (Hildreth and Moorbath, 1988; Hildreth et al., 2010). Cenozoic rocks crop out in the western flank of the Andes Cordillera, corresponding mainly to volcano-sedimentary and volcanic units that cover Mesozoic marine and continental sedimentary formations (Hildreth et al., 2010) (Fig. 1A).

The Laguna del Maule Volcanic Complex constitutes the largest volume of postglacial rhyolites in the Andes (~40 km^3), formed during recent explosive and effusive eruptions (Hildreth et al., 2010; Singer et al., 2014; Wespestad et al., 2019). The volcanic complex covers an area of approximately 500 km^2 with a 15- × 20-km volcanic caldera centered near the northern edge of the Laguna del Maule lake (Fig. 1) and is considered one of the most hazardous active volcanic systems in the Southern Andean volcanic zone. Its eruptive activity began 1.5 m.y. ago with the formation of the Bobadilla caldera (Fig. 1A), and the last effusive eruption occurred about 2 k.y. ago (Andersen et al., 2017). At least 50 eruptions have been documented, forming more than 36 rhyolitic and rhyodacitic domes (Hildreth et al., 2010; Singer et al., 2014, 2018).

Two main structures are recognized in the area: the Troncoso and Laguna Fea faults (Fig. 1A). The dextral strike-slip, N45°E-trending Troncoso fault extends for 30 km to the southwest from the Laguna del Maule lake coinciding with a wide and deep valley known as Cajón Troncoso (Fig. 1A). This fault probably extends to the northeast into the Potrero Norte area (Cardona et al., 2018). The normal W-NW–trending Laguna Fea fault has been inferred through seismic studies and is postulated to intersect the Troncoso fault southwest of the Laguna del Maule lake (Fig. 1A) (Cardona et al., 2018).

Based on detailed studies of postglacial volcanic units of the last 25 k.y., several authors have concluded that the eruptions derive from an integrated silicic magma system (Andersen et al., 2013, 2017; Singer et al., 2014, 2018). Recent geophysical studies using high-precision global positioning systems (GPS) and synthetic aperture interferometric radar (InSAR) techniques have detected a significant volume change below the Laguna del Maule Volcanic Complex, representing one of the largest vertical deformations registered in a volcanic complex (Fournier et al., 2010; Feigl et al., 2014; Le Mével et al., 2016;

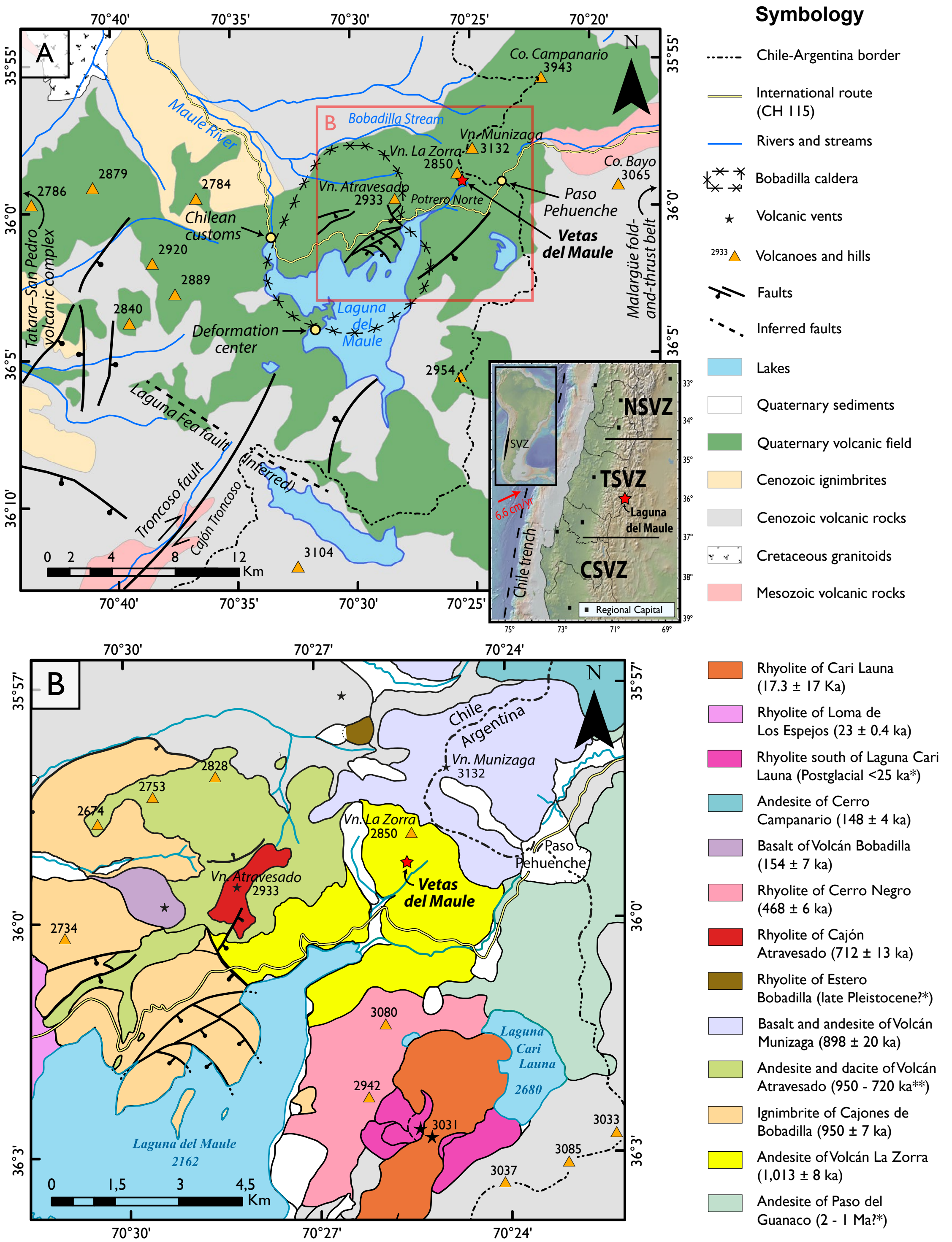

Fig. 1. (A) Location and geologic map of the Laguna del Maule Volcanic Complex. CSVZ = Central Southern volcanic zone, NSVZ = Northern Southern volcanic zone, SVZ = Southern volcanic zone, TSVZ = Transitional Southern volcanic zone. (B) Main volcanic units of the northeast area of the Laguna del Maule Volcanic Complex. Modified from Hildreth et al. (2010), Feigl et al. (2014), and Cardona et al. (2018). ^{40}Ar/^{39}Ar ages are from Hildreth et al. (2010). *Stratigraphic age. **K/Ar age.

Singer et al., 2018; Novoa et al., 2019). This phenomenon has been interpreted as caused by inflation of a shallow magmatic sill and/or injection of hydrothermal fluids under the southwest edge of the Laguna del Maule lake (Feigl et al., 2014; Le Mével et al., 2016).

The Vetas del Maule magnetite mineralization is hosted within the La Zorra volcano, in the northeastern part of the Laguna del Maule Volcanic Complex (Hildreth et al., 2010; Figs. 1B, 2). This volcano is a highly eroded volcanic edifice composed of andesites with 58 to 62 wt % SiO_2 that have been dated at 1.013 ± 0.028 Ma (^{40}Ar/^{39}Ar plateau age; Hildreth et al., 2010). Other adjacent volcanic units also dated by using ^{40}Ar/^{39}Ar methods range from ~0.95 to 0.47 Ma (Hildreth et al., 2010; Fig. 1B). Previous works have identified an ~25-km^2 area of moderate to intense argillic alteration affecting the andesites of the La Zorra volcano. Hydrothermal alteration of the andesites is controlled by the inferred extension of the Troncoso fault and is represented by N65°E-trending veinlets composed by quartz-jarosite-kaolinite-smectite-pyrite and abundant clay alteration (Hildreth et al., 2010; Rojas et al., 2022).

Samples and Methods

Sampling was conducted over the course of three field campaigns. Because of the steep topography of the study area (Fig. 2A), an aerial drone was used to obtain images of the outcrops and build a digital elevation model of the La Zorra volcano (Fig. 2B). We used a DJI Mavic 2 Pro quadcopter equipped with a 20 MP camera. The flight was open planned and operated using DroneDeploy. The software Agisoft Metashape Professional and ArcGIS arcScene were used to reconstruct the 3-D digital elevation model (Fig. 2B). The drone was flown at a speed of 12 m/s and an elevation of 450 to 500 m, and images were obtained with a lateral and longitudinal overlap of 65%. The average size of the images was 5,472 × 3,648 pixels, and each image was automatically georeferenced with 3-D coordinates from the drone GPS.

Surface samples were collected at altitudes between 2,400 and 2,850 m above sea level (a.s.l.) from outcrops on the southwest and southeast slopes of La Zorra volcano (Fig. 2A, B). Nearly all samples are from the inner southeast slope, where most of the mineralization—magnetite, actinolite, and pyroxene breccias, veins, and disseminated grains—was found. Polished thin sections were prepared for polarized-light microscopy, SEM inspection and EMP analysis. Carbon-coated polished thin sections were studied by using a FEI Quanta 250 SEM at the Andean Geothermal Center of Excellence (CEGA), Department of Geology, Universidad de Chile. The SEM instrument was used to characterize textural relationships, zoning patterns, mineral inclusions, exsolutions, and overgrowths, with an emphasis on magnetite. Backscattered electron (BSE) images were obtained using an accelerating voltage of between 15 and 20 kV, a filament current of 80 µA, a beam intensity of ~1 nA, a spot size of 5 µm, and a working distance of 10 mm.

EMPA of magnetite was carried out using a JEOL JX-A8530F Plus field emission electron microprobe equipped with five tunable wavelength dispersive spectrometers located at the Centre of Microscopy, Characterisation and Analysis (CMCA) of the University of Western Australia in Perth, Western Australia. The accelerating voltage was 20 kV, and a focused beam (~1 µm) was set to avoid hitting inclusions and thin exsolution lamellae. Interference corrections were carried out for Ti concentrations because V Kβ affects the Ti Kα signal. The beam current was set to 40 to 50 nA. A counting time of 20 s was used for Fe, while higher counting times were used for the other elements: 30 s for Na and K, and 60 s for Si, Al, Mg, Ti, Ca, Fe, Cr, Ni, V, Mn, Zn, and Cu. Background corrections for all elements were made by using the mean atomic number (MAN) method of Donovan and Tingle (1996). Additionally, quantitative WDS maps of Cr, Ca, Mn, Si, Na, Al, V, Ti, and Mg were obtained on selected magnetite grains. Operating conditions were 40° takeoff angle, and a beam energy of 20 keV was used. The beam current was 50 nA, and counting times were 20 to 60 ms/step. ZAF corrections were applied for all elements, and interference corrections were performed for Fe Kα and V Kα because of Mn K and Ti Kβ interference, respectively. The standards used for both EMPA and WDS included natural and synthetic oxides and silicates (App. Table A1).

Phlogopite separates selected for ^{40}Ar/^{39}Ar dating were obtained from a sample with abundant disseminated magnetite associated with the massive magnetite mineralization (sample MLZ-18). Phlogopite grains (500–1,000 µm) were separated from the crushed/sieved material, washed ultrasonically in deionized water for 10 min, and then handpicked under a binocular microscope to remove any crystals that had visible inclusions or adhered material. Purified separates were placed in a 2.5-cm aluminum disk and irradiated in the cadmium-lined in-core tube at the Oregon State University reactor for 2 h. The 1.1864 Ma Alder Creek sanidine (FCs) (Jicha et al., 2016) was used as a neutron fluence monitor. J values were interpolated geometrically across each 2.5-cm-diameter irradiation disk based on numerous single crystal measurements of FCs, which was distributed in eight to 10 positions within each disk.

Ten phlogopite crystals (~2 mg) were loaded into a 2-mm-diameter well within a copper tray and incrementally heated with a 55-W CO_2 laser in the WiscAr Laboratory at the University of Wisconsin-Madison. The extracted gas was purified via exposure to two SAES GP50 getters in series (both at 50 W/400°C) for 90 s each and to an ARS cryotrap (at –125°C) for another 60 s. Argon isotope analyses were carried out using a Nu Instruments Noblesse multicollector mass spectrometer. Sample analysis consisted of a continuous measurement for ~1,200 s, whereas blank and gas cocktail measurements were made with a peak hop routine described in Jicha et al. (2016). All of the ^{40}Ar/^{39}Ar ages were calculated using the decay constants of Min et al. (2000), and the plateau and isochron ages are reported with 2σ analytical uncertainty, which includes the J uncertainty. All data were reduced and plotted using Pychron software (Ross, 2019).

Results

Magnetite mineralization styles

The IOA-type mineralization recognized at the inner southeast slope of the La Zorra volcano comprises magnetite, actinolite, and pyroxene occurring in breccias and veins and as disseminated grains or aggregates. The mineralization is hosted in andesites that exhibit widespread moderate to pervasive albitization, visible as numerous whitish patches of ~10 to 12 m^2, covering the entire slope (Fig. 2B). Albitization increases in intensity around magnetite mineralization. Overall, five mineralization styles were identified and are described below (Figs. 3–5).

Massive magnetite: An outcrop of ~85 m^2 of decimeter- to meter-scale, irregular, massive magnetite occurs near the top of La Zorra southeast slope at an altitude of ~2,730 m a.s.l. (Figs. 2B, 3A). The orebodies display sharp contacts with the andesitic host rock (Fig. 3B) and are composed of approximately 95% magnetite with minor amounts of ilmenite, rutile, clinopyroxene (augite), orthopyroxene (hypersthene), and apatite. Phlogopite occurs at the margins of the magnetite body (Fig. 4A). Magnetite textures show (1) thin (~0.5–2 μm) ilmenite oxyexsolutions configuring a trellis texture (Fig. 5A), (2) thin (~10–75 μm) alternating inclusion-rich and inclusion-poor bands (Fig. 5C), and (3) irregular inclusion-rich zones (Fig. 5D). Disseminated magnetite aggregates are found occasionally within the andesite host rock, near the contacts with the magnetite orebodies.

Pyroxene-actinolite-magnetite veins: Pale- to dark-green pyroxene-actinolite-magnetite veins were found in close spatial association with the massive magnetite bodies described above (Fig. 2B, D). The veins have thicknesses ranging from a few decimeters up to a couple of meters and run sinuous-

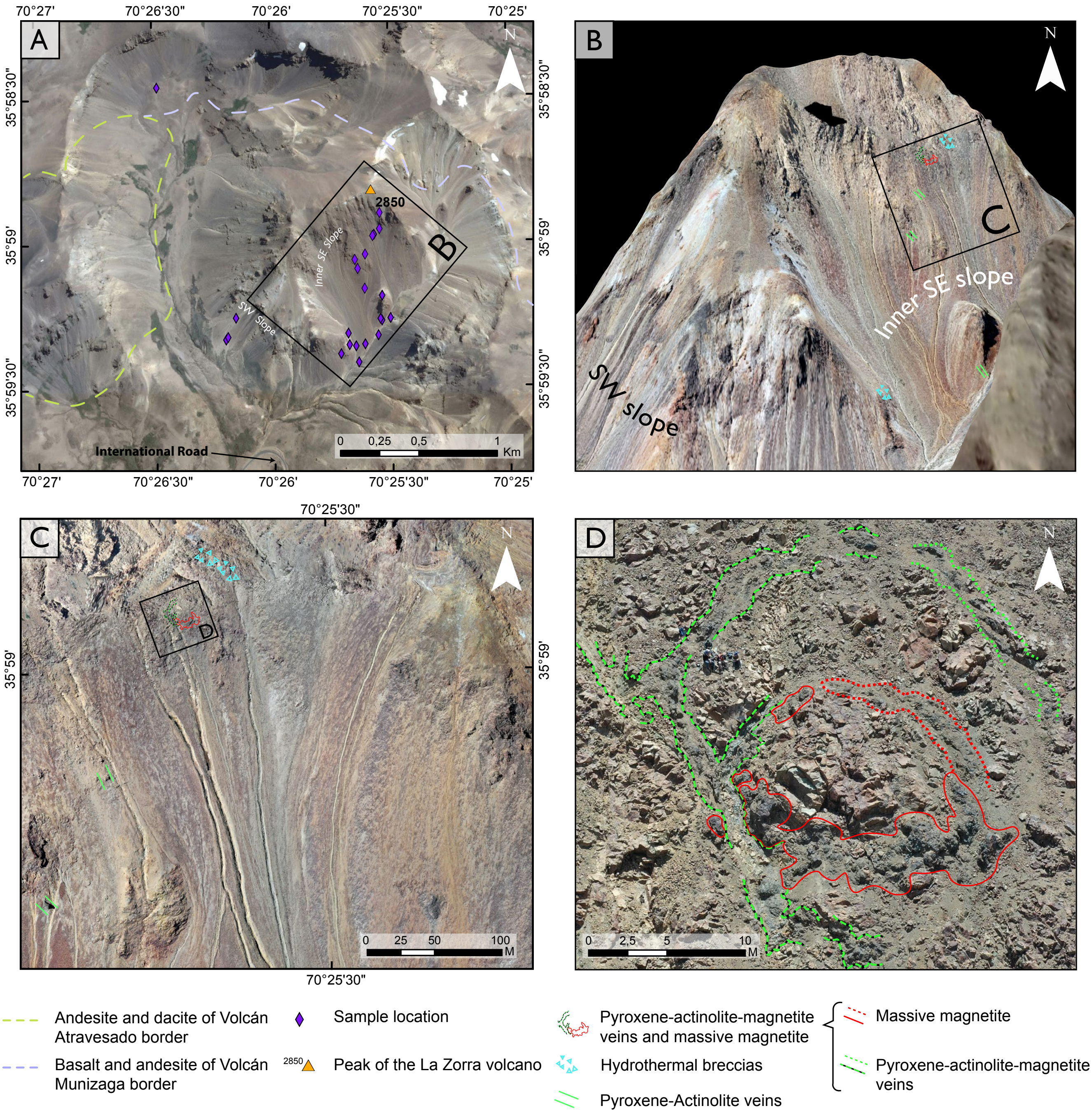

Fig. 2. Location of the Vetas del Maule IOA-type mineralization within La Zorra volcano, Laguna del Maule. (A) Satellite image of the La Zorra volcano dissected by a steep alluvial valley and covered by nearby volcanic units (dashed lines). (B) Aerial drone image of the volcano showing the spatial relationship between the different mineralization styles. The vertical axis is exaggerated (2.5×). (C) Aerial drone image of the easternmost section of the inner southeast slope of the volcano. (D) Aerial drone image of the massive magnetite and pyroxene-actinolite-magnetite veins showing their close spatial relationship.

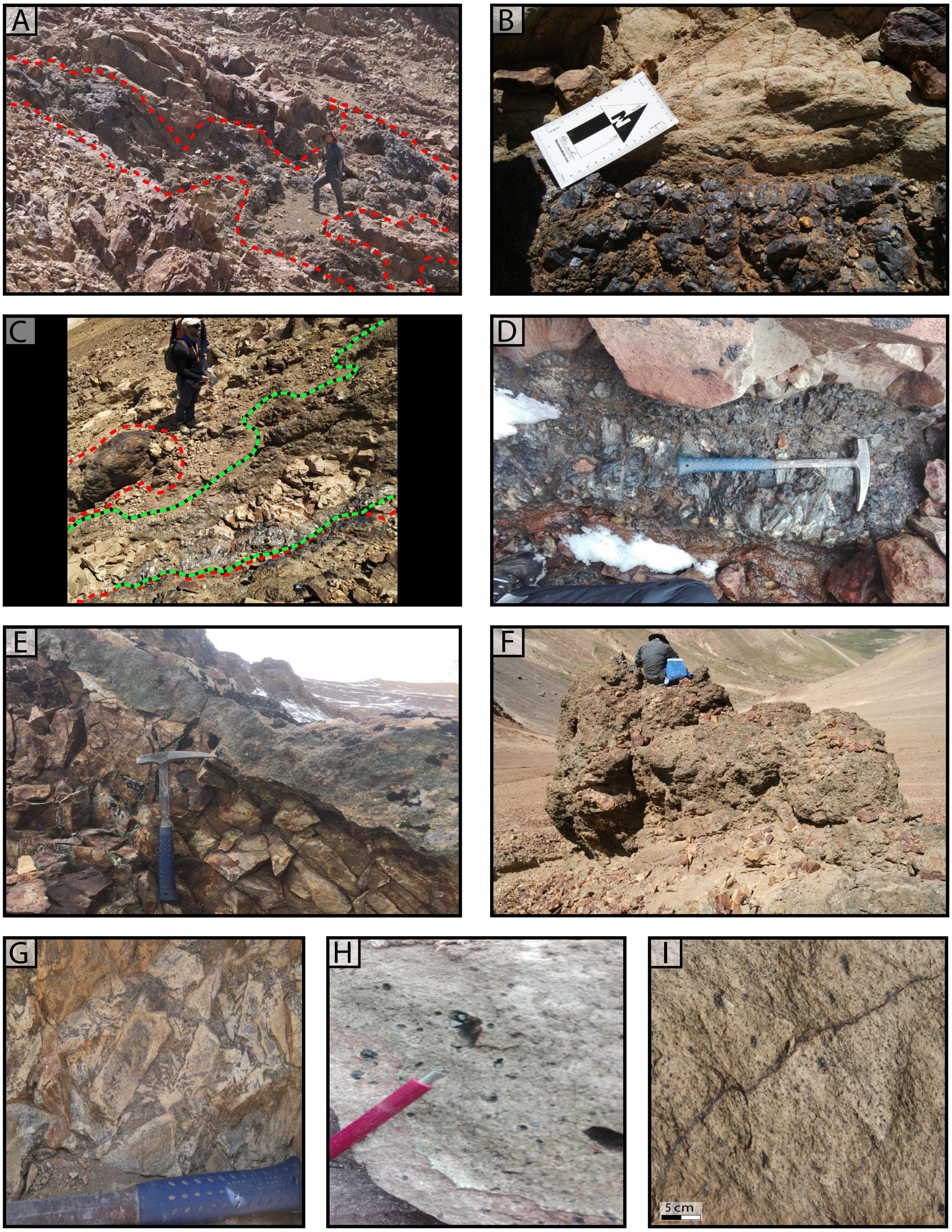

Fig. 3. Field photographs showing the magnetite mineralization styles at Vetas del Maule. (A) Outcrop of the massive magnetite body (red dashed line). (B) Sharp contact between the massive magnetite body and the albitized andesite host rock. (C) Massive magnetite (red dashed line) and pyroxene-actinolite-magnetite veins (black and green dashed line). (D) Thick pyroxene-actinolite-magnetite vein in andesite. (E) Pyroxene-actinolite vein located at the base of the southeast slope. (F) Massive outcrop of pyroxene-actinolite. (G) Easternmost outcrop of hydrothermal breccias. (H) Disseminated magnetite within the andesite host rock. (I) Thin magnetite veinlets.

ly for about 30 m downslope, in some cases bifurcating and surrounding andesite blocks (Figs. 2D, 3C). These veins are formed by an intergrowth of large (~500 μm) crystals of orthopyroxene (hypersthene), clinopyroxene (augite), and actinolite and ~40 to 60% magnetite with minor apatite, ilmenite, and chlorite arranged in comb-like textures (Figs. 3D, 4B). Pyroxene is more abundant than actinolite and is observed with relatively fresh cores and often altered rims to irregular fibrous masses of an Mg-Fe-Si-O phase, probably cummingtonite. Magnetite textures are similar to those described for

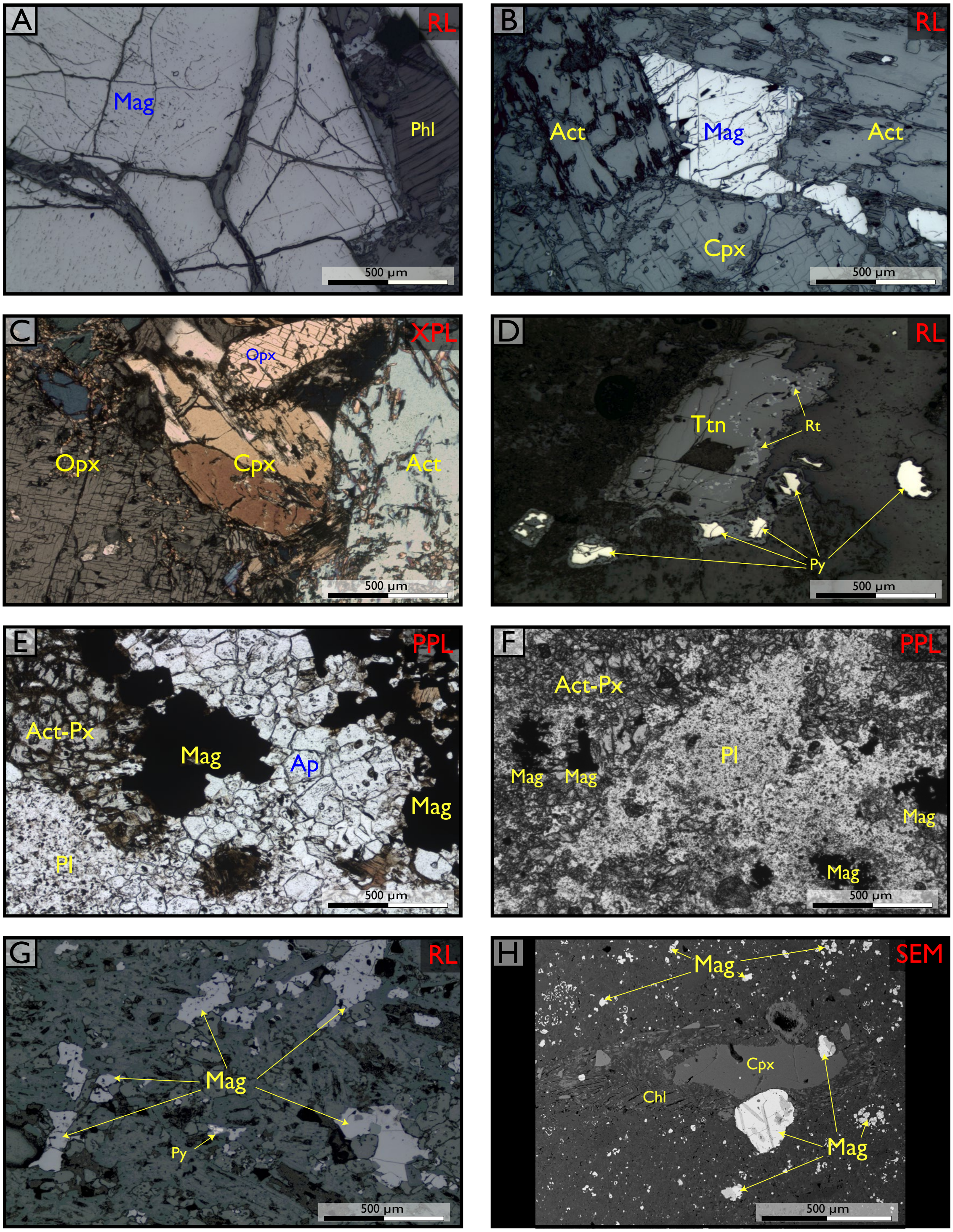

Fig. 4. Photomicrographs of Vetas del Maule IOA-type mineralization. (A) Large magnetite crystal in contact with phlogopite. Massive magnetite sample MLZ-04-B. (B) Pyroxene, actinolite, and magnetite assemblage. Pyroxene-actinolite-magnetite vein sample MLZ-09. (C) Coarse-grained pyroxene and actinolite. Pyroxene-actinolite vein sample MLZ-24-A. (D) Subhedral titanite crystal with small rutile grains and associated pyrite grains. Pyroxene-actinolite vein sample MLZ-03-A. (E) Coarse-grained pyroxene, actinolite, chlorite, magnetite, apatite, and plagioclase. Hydrothermal breccia sample MLZ-26. (F) Fine-grained pyroxene, actinolite, chlorite, magnetite, and plagioclase. Hydrothermal breccia sample MLZ-27. (G) Anhedral magnetite grains disseminated within the andesite groundmass. Disseminated magnetite sample MLZ-08. (H) Clinopyroxene altered to chlorite and abundant disseminated magnetite grains. Disseminated magnetite sample MLZ-12. Abbreviations: Act = actinolite, Ap = apatite, Chl = chlorite, Cpx = clinopyroxene (augite), Mag = magnetite, Opx = orthopyroxene (hypersthene), Phl = phlogopite, Pl = plagioclase (andesine-oligoclase in anhedral matrix), PPL = plane-polarized light, Px = pyroxene, Py = pyrite, RL = reflected light, Rt = rutile, SEM = scanning electron microscope, Ttn = titanite, XPL = crossed nicols.

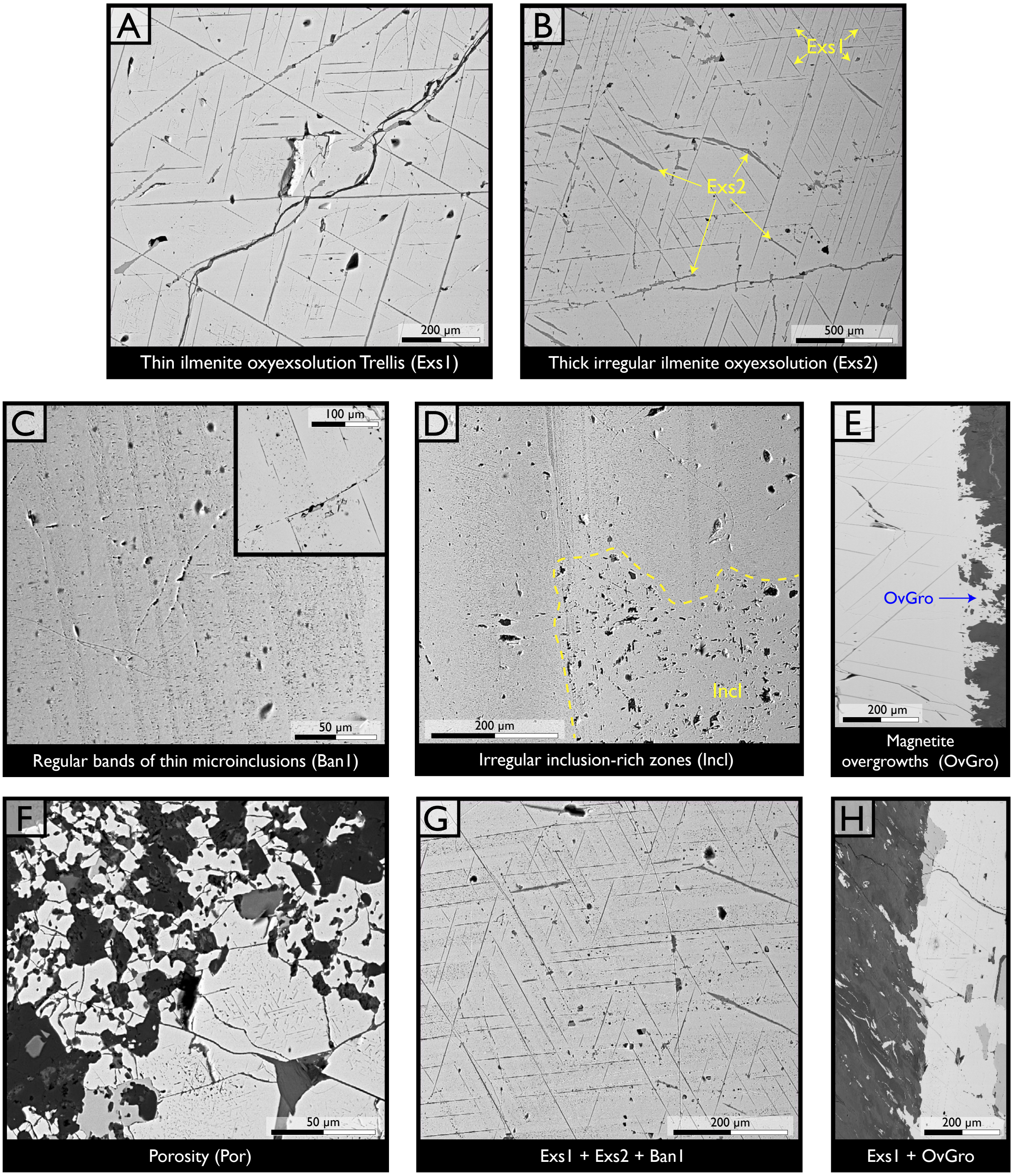

Fig. 5. Backscattered electron images of magnetite textures. Inset in (C) shows thin ilmenite oxyexsolutions aligned with the direction of the regular bands of thin microinclusions. (A), (B), (E), (G), and (H) are from pyroxene-actinolite-magnetite vein sample MLZ-09. (C) and (D) are from massive magnetite sample MLZ-04-B. (F) is from hydrothermal breccia sample MLZ-02.

the massive magnetite bodies (Fig. 5A-D), including thin and thick ilmenite lamellae. Thin alternating bands of microinclusions and irregular inclusion-rich zones are also recognized. Some magnetite grains display late magnetite overgrowths (Fig. 5E).

Pyroxene-actinolite veins: Three pyroxene-actinolite veins were observed along the inner southeast slope of the La Zorra volcano (Fig. 2B). All three have an approximate north-northwest orientation. The first vein is located at ~2,400 m a.s.l., near the base of the southeast slope and is approximately half a meter thick and ~15 m long (Figs. 2B, 3E). The second is a ~2- × 6-m remnant of a larger NNW-trending vein found at ~2,600 m a.s.l. and located at the middle of the inner southeast slope (Figs. 2B, C, 3F). The third is a small, 1-m-thick vein a couple of meters long at about the same altitude as the previous vein (Fig. 2B, C). All three veins display sharp contacts with the andesite host rock. Pyroxene-actinolite veins contain euhedral to subhedral crystals of orthopyroxene (hypersthene), clinopyroxene (augite), and actinolite (Figs. 3E, F, 4C). Minor pyrite, quartz, apatite, calcite, titanite, ilmenite, and magnetite were also observed, as well as a few grains of zircon and thorite. Pyroxene and actinolite display variable degrees of chloritization. Titanite grains are common and replace ilmenite and rutile (Fig. 4D). There is almost no magnetite in the samples (<2%), and when present it appears as pristine, anhedral grains or occasionally with porous texture at the grain rims.

Magnetite hydrothermal breccias: Two outcrops of hydrothermal breccias were identified: one at an altitude of 2,800 m a.s.l., ~80 m to the east of the massive magnetite outcrop located at the inner southeast slope, and the second at a lower altitude (~2,450 m a.s.l.; Fig. 2B, 3G). The breccias occur as irregular decimeter to decameter masses and are composed of angular and rounded clasts of albitized andesite, immersed in a fine-grained dark-green matrix consisting of ~30 to 80% magnetite, pyroxene, actinolite, chlorite, apatite, and minor ilmenite and pyrite (Fig. 4E, F). Magnetite in the breccia matrix shows different forms of ilmenite lamellae in anhedral grains. Thin-banded textures as well as porous magnetite were also observed (Fig. 5A-C, F). For the sake of simplicity, the magnetite hydrothermal breccias will be referred to as "hydrothermal breccias" throughout the text.

Disseminated magnetite: Disseminated magnetite grains that are tens of micrometers to centimeters in size are observed in the host rock adjacent or close to the magnetite mineralization and are especially abundant near to hydrothermal breccias (Fig. 3H, I) and absent around pyroxene-actinolite veins. Most occurrences are characterized by anhedral magnetite grains dispersed within albitized andesite (Fig. 4G, H), although often they occur as euhedral crystals filling vesicles (Fig. 3H). In some cases, the disseminated magnetite is closely related to occasional occurrence of thin (tens of micrometers to centimeters thick) veinlets of magnetite (Fig. 3I). Magnetite grains show thin and thick ilmenite oxyexsolution lamellae and often porosity restricted to grain rims (Fig. 5A, B, F).

Figure 6 summarizes the sequence of mineral formation or paragenesis for Vetas del Maule. In addition, a table summarizing the mineralogical characteristics of the different styles is presented in Appendix Figure A1. In the latter, further descriptions of each mineralization style are presented, including individual textures of magnetite, as well as combinations of different magnetite textures observed in BSE images.

Magnetite geochemistry

EMPA data: Figure 7 displays magnetite EMPA data presented as box plots for each mineralization style. Additionally, and for more detail, concentration plots for each major, minor, and trace element in magnetite are plotted in Appendix Figure A2 as a function of the different magnetite microtextures observed within each mineralization style. All EMPA data are reported in Appendix Tables A2 and A3, respectively.

Most elements analyzed in magnetite—i.e., Si, Na, Al, Mg, Ti, and V—exhibit variable concentrations, ranging between ~25 and 100 ppm (mean detection limits), up to a few weight percent. Potassium, Mn, and Ca, on the other hand, display lower concentrations, generally not exceeding 0.3 wt %. Nickel, Cr, Cu, and Zn are rarely detected. Although no apparent trends are observed between element concentrations and individual textures in the different mineralization styles, it is noted that exsolution and banded textures—and their combinations— show high compositional variability (App. Fig. A2).

Among all mineralization styles, magnetite in massive magnetite and pyroxene-actinolite-magnetite veins exhibits the highest mean concentrations of Mg (1.06 and 0.98 wt %, respectively), Na (0.26 and 0.16 wt %, respectively), Si (0.28 and 0.29 wt %, respectively), and Mn (both 0.08 wt %). Magnetite in these styles also presents relatively high concentrations of V (mean concentration of 0.31 and 0.41 wt %, respectively), K (0.01 and 0.02 wt %, respectively), and Ca (0.04 and 0.08 wt %, respectively); both styles are enriched with respect to two of the other three styles. On the other hand, magnetite in the disseminated magnetite and pyroxene-actinolite veins styles is depleted in Mg (mean concentration of 0.14 and 0.11 wt %, respectively), Na (0.04 and 0.03 wt %, respectively), Si (0.12 and 0.11 wt %, respectively), and Mn (0.04 and 0.02 wt %, respectively), and most samples have low K (generally near detection limit). Magnetite in the pyroxene-actinolite veins is also depleted in Al (mean concentration of 0.02 wt %), Ti (0.06 wt %), and V (0.12 wt %) when compared to the other styles, while most samples of disseminated magnetite grains are depleted in Ca (generally <0.01 wt %). Finally, and relative to other mineralization styles, magnetite in the hydrothermal breccias exhibits intermediate concentrations of K (generally <0.02 wt %), Mg (mean concentration of 0.28 wt %), Al (0.43 wt %), and Mn (0.05 wt %) and is depleted in Ca (0.03 wt %), Na (0.03 wt %), Si (0.11 wt %), and V (0.11 wt %), with concentrations similar to those of magnetite in the disseminated magnetite and/or pyroxene-actinolite (Fig. 7). Overall, aluminum mean concentrations in magnetite are similar between all mineralization styles (around 0.41 wt %), with the exception of the pyroxene-actinolite veins (below detection).

The EMPA magnetite data were plotted in the Fe vs. (V/Ti) diagram of Wen et al. (2017) (Fig. 8). Most data points fall within the right part of the diagram, with Fe concentrations ranging between ~66 and 72 wt %. Magnetite data tend to group with mineralization style and texture. For example, magnetite in the pyroxene-actinolite-magnetite veins, pyroxene-actinolite veins, and massive magnetite bodies shows the highest V/Ti ratios (0.7–10), followed by disseminated magnetite with intermediate V/Ti values (0.3–3); hydrothermal breccias have V/Ti < 0.5 (Fig. 8). Notably, only a few magnetite data points from all styles—with the exception of magnetite in the pyroxene-actinolite veins—plot in the bottom-left part of the diagram.

^{40}Ar/^{39}Ar ages: Phlogopite separates were obtained from a sample with abundant disseminated magnetite, associated with massive magnetite mineralization (sample MLZ-18). The phlogopite grains were analyzed by step heating using a CO_2 laser and a multicollector mass spectrometer. A total of 18 heating steps were performed for the phlogopite sample, yielding a concordant plateau age of 873.6 ± 30.3 ka (2σ), identical within error to the calculated inverse isochron age of 861.3 ± 45.1 ka (2σ). The isochron has a ^{40}Ar/^{36}Ar intercept that is indistinguishable from the atmospheric value, indicat-

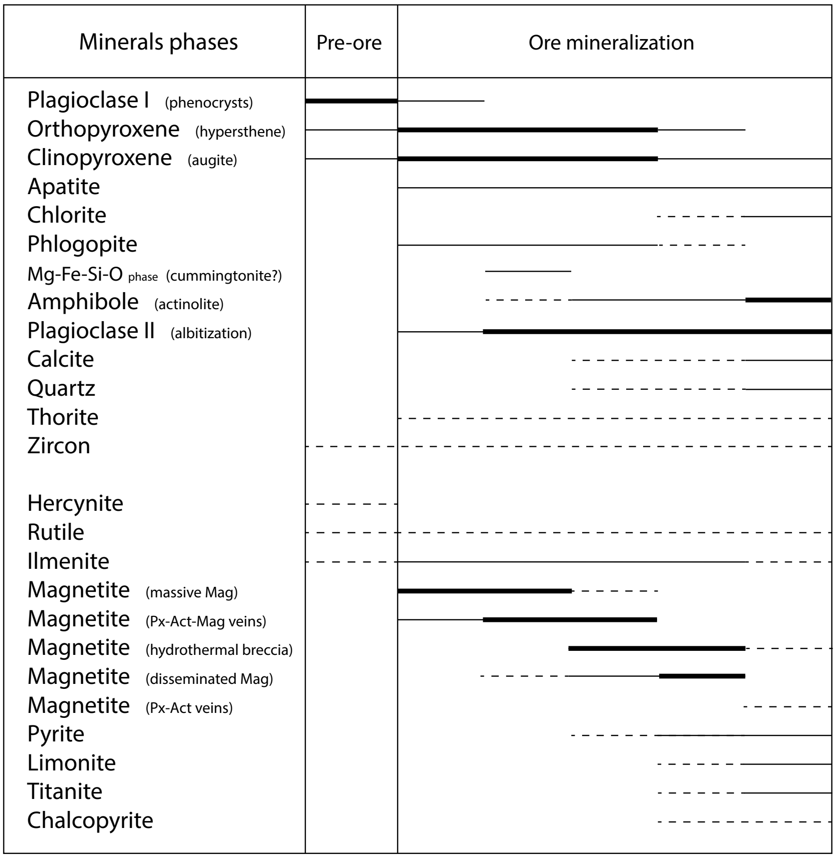

Fig. 6. Paragenetic scheme showing the sequence of mineral formation. Magnetite types were differentiated according to their occurrence in each mineralization style. The thickness of the line is proportional to the relative abundance of the mineral. The dashed line indicates a low presence of the mineral. Abbreviations: Act = actinolite, Mag = magnetite, Px = pyroxene.

ing that trapped excess Ar is not present in the sample. The age spectra diagram and isotope correlation plot are shown in Appendix Figure A3. All ^{40}Ar/^{39}Ar data including interference corrections are reported in Appendix Table A4.

Discussion

Origin of the magnetite

The different styles of magnetite mineralization identified at Vetas del Maule share similar compositional and textural features with IOA or Kiruna-type deposits worldwide, especially those in the Coastal Cordillera of northern Chile and the Pleistocene El Laco deposit in the Chilean Altiplano. These deposits display similar mineralization styles including massive magnetite bodies, and hydrothermal breccias and veins, as well as disseminations and extensive alteration zones in the volcano-sedimentary host rocks (Sillitoe, 2003; Williams et al., 2005; Barton, 2014; Barra et al., 2017; Ovalle et al., 2018; Simon et al., 2018; Palma et al., 2020; Reich et al., 2022; Zhao et al., 2024).

Magnetite is ubiquitous in several types of mineralized systems, and, therefore, its trace element geochemistry has been extensively investigated in IOA, Fe-Ti, V (nelsonite), porphyry Cu, skarn, IOCG, volcanogenic massive sulfide, and banded iron formation deposits, among others (e.g., Dupuis and Beaudoin, 2011; Nadoll et al., 2014; Dare et al., 2015; Knipping et al., 2015a, b; Makvandi et al., 2016; Hawkins et al., 2017; Wen et al., 2017; Huang and Beaudoin, 2019; Palma et al., 2020; Hu et al., 2022; McCurdy et al., 2022; Sullivan et al., 2023). Those studies have used the concentration of key elements such as Fe, Ca, Al, Mn, Mg, Ga, Ti, and V to identify akin geochemical signatures of magnetite in various deposits, which are useful in exploration. They also qualitatively infer the physicochemical conditions of magnetite formation, e.g., temperature and oxygen fugacity, among other factors.

As described in the results, there is considerable variability in the concentration of most elements among the different mineralization styles observed in magnetite at Vetas del Maule (Fig. 7). Some of this compositional variability seems to be related to the influence of the magnetite microtextures (Fig. 8; App. Fig. A2). In compositional diagrams, data with the same microtexture within the same sample are grouped into clusters that are distinguishable from those with other microtextures (Fig. 8; App. Fig. A2). For example, for Na, V, and K, the samples with oxyexsolutions and rhythmic banding (Exs1 + Ban1) show different concentration ranges among mineralization styles. However, almost all microtextures, including oxyexsolutions and rhythmic banding, observed within the same mineralization style (e.g., hydrothermal breccia) can be grouped into similar compositions (App. Fig. A2). In summary, the composition of magnetite is primarily controlled by the mineralization style of the sample, rather than

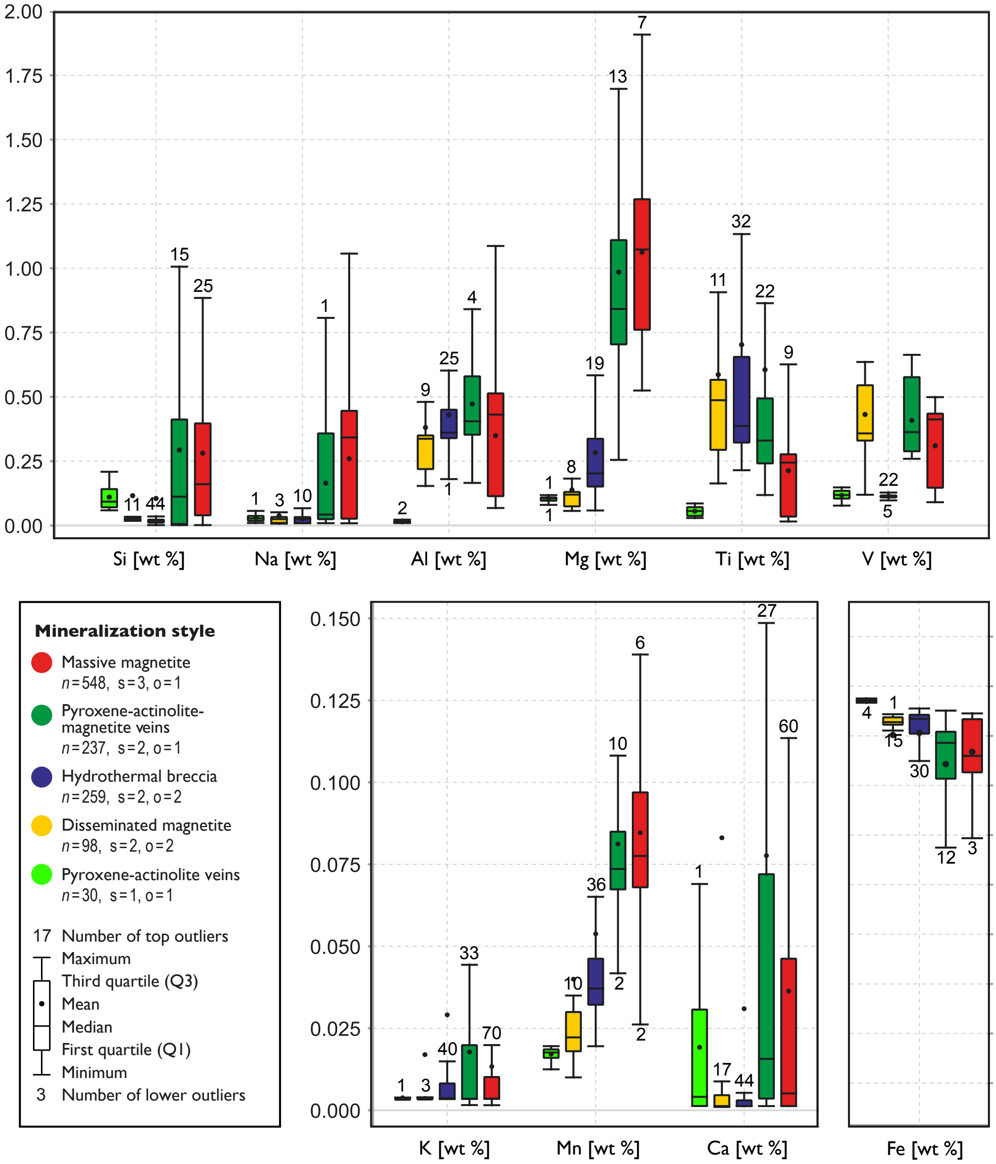

Fig. 7. Concentration plot for major, minor, and trace elements in magnetite from the different mineralization styles at Vetas del Maule. Electron microprobe analysis (EMPA) spot data are included for each mineralization style, i.e., massive magnetite (red), pyroxene-actinolite-magnetite veins (dark green), hydrothermal breccia (blue), disseminated magnetite (yellow), and pyroxene-actinolite veins (light green). Abbreviations: *n* = number of spot analyses, o = number of outcrops from where the samples were obtained, s = number of samples analyzed.

by microtextures. Furthermore, and as observed in Figure 7, the concentration of several elements in magnetite from Vetas del Maule—most notoriously Mg, Na, Si, and Mn, and less evidently V, Ca, and potassium—configures a trend that varies from trace element-rich magnetite (e.g., massive magnetite and/or pyroxene-actinolite-magnetite veins), through magnetite with (variable) intermediate trace element concentrations (e.g., hydrothermal breccias), to trace element-poor magnetite (e.g., disseminated magnetite and/or pyroxene-actinolite veins styles). Conversely, Fe concentrations follow the opposite trend, reflecting a greater incorporation of trace elements into the magnetite structure with decreasing Fe contents (Fig. 7). This is consistent with common Fe^{2+}-Fe^{3+} cationic substitution mechanisms occurring in the octahedral sites of magnetite, which are in turn sensitive to temperature—meaning that magnetite with lower trace element content would form at lower temperatures and vice versa (Nadoll et al., 2014; Canil and Lacourse, 2020).

Such elemental variations in magnetite have also been reported in several ore systems, including other IOA deposits, and are likely associated with cooling from high-temperature magmatic-hydrothermal conditions (600°–1,000°C) to lower-temperature hydrothermal conditions (<600°C) (Nadoll et al., 2014; Knipping et al., 2015b; Ovalle et al., 2018; Rojas et al., 2018; Palma et al., 2020, 2021; Salazar et al., 2020; Zhao et al., 2024). This suggests that the different magnetite types identified at Vetas del Maule may have formed at different temperatures and evolving physicochemical conditions.

Further understanding of the formation conditions of magnetite mineralization at Vetas del Maule can be obtained from

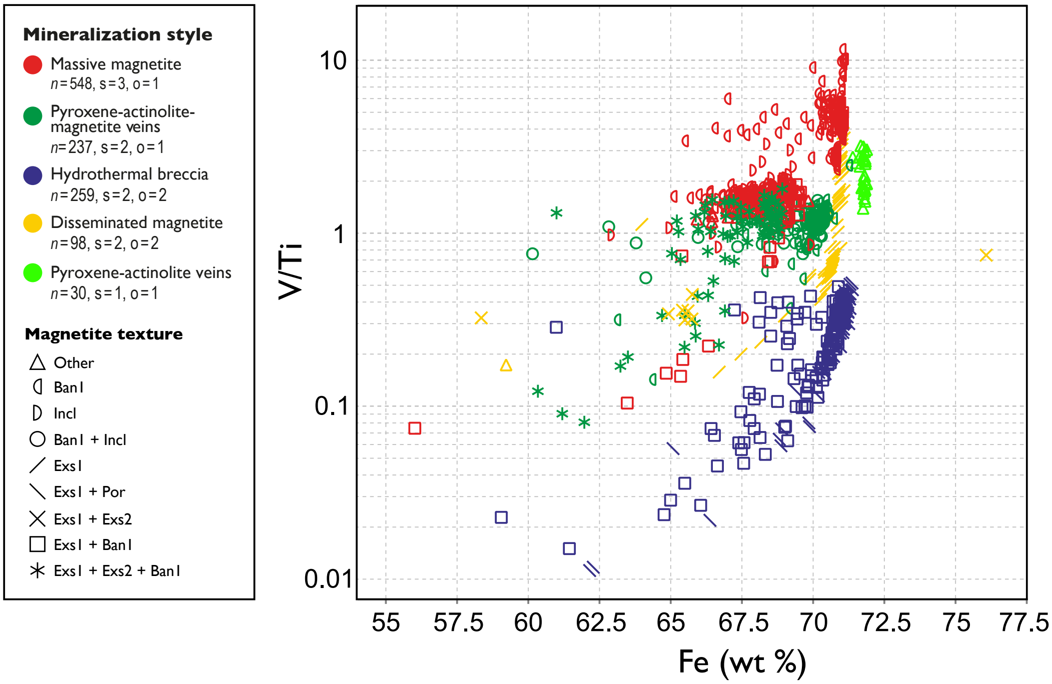

Fig. 8. Fe vs. V/Ti discriminant diagram for magnetite with magmatic and hydrothermal fields, as proposed by Wen et al. (2017). Magnetite microtextures are indicated using symbols. Abbreviations: Ban1 = regular bands of thin microinclusions, Exs1 = thin ilmenite oxyexsolution trellis, Exs2 = thick irregular ilmenite oxyexsolution, Incl = irregular inclusion-rich zones, *n* = number of spot analyses, o = number of outcrops from where the samples were obtained, Por = porosity, s = number of samples analyzed.

the Fe vs. V/Ti diagram by Wen et al. (2017). In Figure 8, magnetite data configure distinctive areas defined primarily by each mineralization style, with some variability within each style according to the microtexture. As described, nearly all magnetite analyses plot in the right part of the diagram, which suggests that magnetite at Vetas del Maule formed from high-temperature hydrothermal fluids. However, it is important to note that discrimination diagrams tend to neglect complex features of trace element substitution mechanisms, as well the initial melt/fluid composition and the partitioning effect of co-crystallizing phases. Furthermore, microtextural features such as ilmenite oxyexsolutions, microinclusions, and/or rhythmic banding in magnetite may have an influence on Fe wt % and V/Ti ratios. Hence, the Wen et al. (2017) diagram must be used with caution to discriminate between hydrothermal vs. magmatic magnetite. In this particular case, our magnetite data suggest that Fe wt % and V/Ti ratios are not significantly affected by microtextures. As described, there is a broad correspondence between Fe-V/Ti data and microtextural types for each magnetite mineralization style (Fig. 8). Furthermore, we note that very few analyses of each mineralization style plot in the bottom-left part of the diagram, interpreted as of magmatic origin in other deposits (Wen et al., 2017; Palma et al., 2020; Reich et al., 2022); these few data points configure a broad trend toward higher V/Ti and Fe concentrations within each style. Similar trends have been described in the literature when magnetite grains undergo reequilibration via fluid-mediated dissolution-reprecipitation processes, reinforcing the argument of the involvement of a hydrothermal fluid (Wen et al., 2017; Deditius et al., 2018; Ovalle et al., 2018, 2022; Huang and Beaudoin, 2019; Palma et al., 2020). Nevertheless, the potential influence of submicrometer-sized inclusions or ilmenite oxyexsolutions on Fe wt % and V/Ti ratios cannot be ruled out completely.

Despite these uncertainties, the proposed involvement of high-temperature hydrothermal fluids at Vetas del Maule is consistent with the described occurrence of magnetite mineralization in veins (Figs. 2D, 3C, D, E, I), breccias (Fig. 3G), disseminations (Fig. 3H), and the ubiquitous albitization on the slope of the volcano that hosts the mineralization (Fig. 2B, C). Further studies including stable isotopic and fluid inclusion analyses are necessary to robustly corroborate this hypothesis.

Magnetite microtextures and reequilibration

As described, magnetite from Vetas del Maule displays complex microtextural characteristics, similar to those reported in several magnetite-bearing ore deposits in Chile and elsewhere (e.g., Knipping et al., 2015a; Wen et al., 2017; Deditius et al., 2018; Ovalle et al., 2018; Rojas et al., 2018; Simon et al., 2018; Huang and Beaudoin, 2019; Palma et al., 2020; Salazar et al., 2020; Ye et al., 2023). Microtextures can provide valuable information to better understand the geochemical trends described for each magnetite type, as well as the potential relationship of magnetite to temperature and redox fluctuations.

In the studied samples, magnetite contains both ilmenite oxyexsolutions and variable amounts of ilmenite grains (Fig. 5; App. Fig. A1). Typically, accessory magnetite with trellis-like ilmenite exsolutions and ilmenite grains has been described in igneous rocks, in magmatic Fe-Ti, V, and Ni-Cu sulfide deposits (Buddington and Lindsley, 1964; Boutroy et al., 2014; Tan et al., 2016), and in a number of magmatic-hydrothermal ore systems, including Fe skarns (Hu et al., 2015; Hawkins et al., 2017; Wen et al., 2017), volcanic-hosted Fe-Cu (Wang et al., 2020), IOCG (Huang and Beaudoin, 2019; Rodriguez-Mustafa et al., 2020), and IOA deposits (Borrok et al., 1998; Ovalle et al., 2018; Parente et al., 2019; Palma et al., 2020).

The presence of two or more types of ilmenite exsolutions coexisting within the same magnetite grain in nearly all mineralization styles points to a complex evolution (Fig. 5B, G). Similar coexistence of various ilmenite exsolution types (e.g., thin oxyexsolution trellis and thick irregular exsolutions) has been observed in magmatic Fe-Ti oxide-bearing intrusions and interpreted as product of different subsolidus exsolution mechanisms—including oxyexsolution of ilmenite and interoxide reequilibration—indicating multiple stages of ilmenite formation under fluctuating temperature and oxygen fugacity conditions (Tan et al., 2016).

At Vetas del Maule, the common presence of thin ilmenite exsolution textures (trellis) is consistent with an oxyexsolution formation mechanism, whereas the occurrence of ilmenite grains adjacent to magnetite and thicker lamellae may indicates interoxide reequilibration processes, similar to those proposed for the lenticular-lamellae described in Tan et al. (2016). In this regard, Ti displays a particularly complex distribution at the grain scale, with Ti-rich domains in magnetite and Ti in ilmenite trellis, probably reflecting multiple superimposed formation processes (Fig. 9A).

Banded textures are also common in the studied samples and provide further insights on magnetite formation conditions. Textures with fine bands (Fig. 5C) show darker-BSE, micro- to nano-sized microinclusion-rich bands that are depleted in Fe (by 1–3 wt %; Fig. 9F) but enriched in Mg, Si (0.1–5 wt %; Fig. 9E, G), Al, Na, and Ca (0.1–1 wt %; Fig. 9C, H) with respect to lighter-BSE, microinclusion-poor bands. In addition, coarser inclusion-rich (up to tens of μm) magnetite grains form irregular zones (Fig. 5D) depleted in Si, Ca, Al, Mg, Mn, and Ti with concentrations of trace elements similar to those of magnetite from the lighter-BSE, microinclusion-poor bands.

Regular bands of microinclusions have been reported in other IOA deposits (e.g., Los Colorados, Carmen, Fresia, and El Laco) and are attributed to magnetite that crystallized from magmatic-hydrothermal fluids (Knipping et al., 2015b; Deditius et al., 2018; Ovalle et al., 2018; Yin et al., 2019; Palma et al., 2020). This texture has been interpreted as originating from fluctuating supersaturation conditions of the mineralizing fluids with respect to oxide and silicate phases. Such conditions can trigger formation of alternate bands rich in mineral micro/nanoinclusions and trace element-poor zones during progressive growth of the hydrothermal magnetite surface (Deditius et al., 2018; Huang and Beaudoin, 2021; Verdugo-Ihl et al., 2021). At Vetas del Maule, it is noted that regular bands of microinclusions were observed in three mineralization styles (massive magnetite, pyroxene-actinolite-magnetite veins, and hydrothermal breccias). These bands occur both alone and coexisting with superimposed ilmenite lamellae within the same magnetite grain (Figs. 5B, G, 9); this texture has been interpreted as formed by a supersaturated Ti-rich fluid that precipitates both microinclusions and titanomagnetite that subsequently exsolved ilmenite lamellae (Tan et al., 2016; Ovalle et al., 2022).

Overgrowth and porous textures in magnetite are also common at Vetas del Maule (Fig. 5E, F). These features are similar to those observed in other IOA deposits and interpreted as the result of dissolution-reprecipitation processes (Putnis, 2009; Ovalle et al., 2018; Huang and Beaudoin, 2019; Palma et al., 2020). During dissolution-reprecipitation, primary igneous magnetite grains can be altered or replaced by microporous magnetite and then reequilibrated as nonporous varieties. The latter appear as pristine euhedral grains (without evident microtextures), have lower concentrations of trace elements and higher Fe contents, and are associated with lower temperatures (<600°C) (Wen et al., 2017). Several authors have related dissolution-reprecipitation textures to new injections of hydrothermal fluids that react with previously precipitated minerals (Putnis, 2009, 2015; Huang and Beaudoin, 2019). The involvement of such fluids would be consistent with the pervasive albitization of the host rock (Fig. 4E, F) and the alteration textures observed in primary silicates (e.g., reaction rims, Fig. 4H). Overall, the observed magnetite microtextures strongly suggest a fluid-dominated system throughout much of the evolutionary history. This process was likely punctuated by several hydrothermal pulses characterized by fluctuating temperature and oxygen fugacity conditions.

Genetic model

The geologic and mineralogical characteristics of mineralized bodies at Vetas del Maule are similar to those described for other Andean IOA deposits. The microscopic features of magnetite in several of these deposits have been interpreted to reflect a transition from high-temperature igneous conditions at depth to lower-temperature magmatic-hydrothermal conditions at shallow levels (Ovalle et al., 2018, 2022, 2023; Rojas et al., 2018; La Cruz et al., 2020; Palma et al., 2020, 2021; Salazar et al., 2020). Regardless of the primary igneous processes that may concentrate Fe in the source magma in IOA systems—i.e., volatile-driven magnetite saturation and flotation (Knipping et al., 2015a, b), Fe-Ca-P liquid immiscibility (Hou et al., 2018; Keller et al., 2022; Tornos et al., 2024), or exsolution of carbonate-sulfate melts (Bain et al., 2020; Xu et al., 2024)—it is well accepted that (saline) hydrothermal fluids are relevant agents of IOA- and IOCG-type mineralization in volcanic arc settings (Sillitoe and Burrows, 2002; Sillitoe, 2003; Barton, 2014; Reich et al., 2022; Zhao et al., 2024).

For Vetas del Maule, mineralogical and geochemical data suggest that mineralization occurred under conditions similar to those of other Andean IOA systems and deposits that have a unambiguous hydrothermal origin—for instance, Fe skarns (Hawkins et al., 2017). The phlogopite ^{40}Ar/^{39}Ar data indicate a magnetite mineralization age of 873.6 ± 30.3 ka for Vetas del Maule (plateau age, App. Fig. A3), the youngest age recorded to date for any IOA type mineralization worldwide. This age is ~120 k.y. younger than the La Zorra andesite host rocks (^{40}Ar/^{39}Ar plateau age of 1013.0 ± 28.0 ka; Hildreth et al., 2010), indicating that the magnetite bodies are closely related to the evolution of the volcano-magmatic system.

Vetas del Maule is an example of IOA-type volcanogenic mineralization that was the result of a sequence of events during the evolution of La Zorra volcano (Fig. 10). The first event

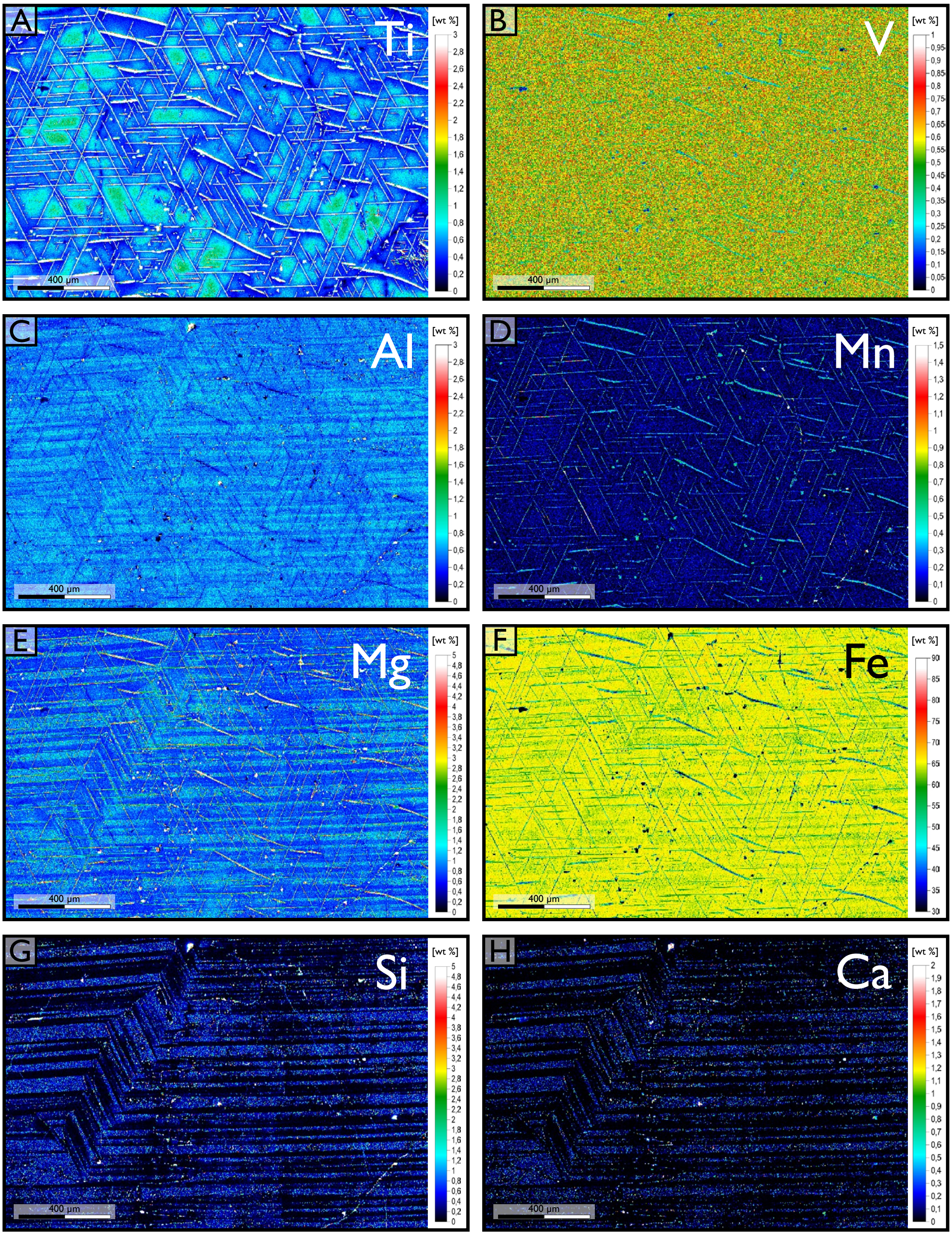

Fig. 9. Quantitative wavelength dispersive spectrometry maps of selected elements in magnetite illustrating the complex elemental distribution associated with the different microtextures. Pyroxene-actinolite-magnetite vein sample MLZ-09, same as Figure 5G. The grain displays superimposed thin ilmenite oxyexsolution trellis, thick irregular ilmenite oxyexsolution, and regular bands of thin microinclusions.

led to the formation of the massive magnetite orebodies, pyroxene-actinolite-magnetite veins, hydrothermal breccias, and disseminated magnetite under conditions typical of a subvolcanic environment (Fig. 10A). These mineralization styles are likely the result of geologic processes involving hydrothermal fluids that were exsolved from a magma reservoir at depth and that were injected upward through fractures in the volcanic edifice. Magnetite in the massive orebodies and pyroxene-actinolite-magnetite veins shows a similar trace element signature, with relative enrichment in Mg, Na, Si, Mn, K, V, and Ca, which is representative of near-igneous temperature conditions (Dupuis and Beaudoin, 2011; Nadoll et al., 2014;

Knipping et al., 2015b; Wen et al., 2017; Ovalle et al., 2018, 2022; Rojas et al., 2018; Palma et al., 2020, 2021; Salazar et al., 2020). These two mineralization styles are found in close spatial association with each other (Figs. 2D, 3C); petrographic observations suggest that the formation of massive magnetite preceded the formation of pyroxene-actinolite-magnetite veins, as evidenced by the absence of actinolite and abundant pyroxene inclusions in the massive magnetite (Fig. 6; App. Fig. A1). This points to conditions above the stability field of actinolite for the massive magnetite orebodies, i.e., ≥780°C at 1 kbar (Lledo and Jenkins, 2008). Furthermore, various pyroxene grains in the pyroxene-actinolite-magnetite veins have rims and fractures altered to irregular fibrous masses of an Mg-Fe-Si-O phase, probably cummingtonite ($Mg_7(Si_8O_{22})(OH)_2$). Experimental studies on the upper thermal limit for Mg-rich actinolite by Lledo and Jenkins (2008) propose the change from [Opx, Cpx, Qz, and H_2O] toward [actinolite] below 780°C at 1 kbar and toward [actinolite + cummingtonite] below 700°C at 1 kbar. In the cited experiments, cummingtonite tends to occur forming similar reaction rims.

The formation of hydrothermal breccias and disseminated magnetite probably occurred at lower temperatures (below ~700°C) and may reflect a change in hydrostatic conditions within the volcanic edifice. Magnetite breccias have been described in other IOA deposits and are interpreted as having been formed by hydraulic injection of hydrothermal fluids under rapid decompression rates (Palma et al., 2020; Ovalle et al., 2022; Zhao et al., 2024). In IOA deposits from the Chilean iron belt, fluid-filled open fractures and breccias indicate that magnetite precipitation was triggered by significant pressure drop at shallow crustal levels, according to mechanisms of brecciation proposed by several authors (Norton and Cathles, 1973; Vargas et al., 1999; Cox et al., 2001; Sibson, 2001; Olivares et al., 2010). Moreover, abrupt pressure changes significantly decrease the solubility of $FeCl_2$ complexes in the fluid, increasing the efficiency of magnetite precipitation (Simon et al., 2004; Rojas et al., 2018; Reich et al., 2022). This is noteworthy at the El Laco deposit, where hydrothermal breccia bodies were ubiquitously observed in drill core samples and were interpreted as having been formed during the collapse of the volcanic edifice (Ovalle et al., 2018, 2022). Thus, it is likely that the hydrothermal breccias at Vetas del Maule are the product of a similar process, i.e., hydraulic injection of hydrothermal fluids with subsequent fracturing and rapid decompression rates.

The precise mechanisms leading to rapid decompression remain unconstrained and could be investigated in future studies. However, possible triggers for decompression may include internal factors related to the magmatic system evolution, such as fluid overpressure (Gudmundsson and Brenner, 2001), or external effects, such as landslide-induced flank collapse (Manconi et al., 2009). Finally, the pyroxene-actinolite veins probably formed during a late or waning stage, characterized by hydrothermal fluids of relatively lower temperature (below ~600°C) that infiltrated other fractures and open spaces (Fig. 10B). Pyroxene-actinolite veins have some distinct characteristics when compared to the other mineralization styles. For example, they appear as isolated veins far from the other mineralization styles and further from the core of magnetite mineralization (Fig. 2B); also, their immediate host rock presents a relatively lower intensity of albitization. Moreover, no disseminated magnetite was found in the vicinity of the veins. This mineralization style also presents higher amounts of actinolite (exceeding pyroxene) and quartz, and titanite is especially abundant in large aggregates associated with minor pyrite and chalcopyrite (Fig. 4D). Most importantly, the pyroxene-actinolite veins contain little magnetite (<2% modal). When present, magnetite in the pyroxene-actinolite veins is trace element poor (except for Ca; Fig. 7) and appears homogeneous or with porous rims. Particularly, the predominance of titanite over ilmenite points to a substantial increase in redox conditions (Xirouchakis et al., 2001a, b; Kohn, 2017). Previous studies have documented that hydrothermal magnetite that formed at low temperatures (e.g., <600°C) has lower concentrations of trace elements and higher Fe contents due to repeated reequilibration associated with coupled dissolution-reprecipitation processes (Wen et al., 2017; Ovalle et al., 2018; Huang and Beaudoin, 2019). All these characteristics indicate abrupt changes in physicochemical conditions and formation under lower temperatures and higher oxygen fugacity, probably in the waning stages of the hydrothermal system.

Finally, the Laguna del Maule volcanic complex experienced significant erosion after glaciers retreated from the area at ~25 ka (Singer et al., 2000). Therefore, recent intense glacial erosion and consequent isostatic rebound during retreat could have exposed these magnetite orebodies at the surface (Fig. 10C).

Notwithstanding the predominantly hydrothermal characteristics described at Vetas del Maule, other genetic mechanisms involving Fe-rich ultrabasic melts and/or molten salts cannot be ruled out (Tornos et al., 2024; Xu et al., 2024). The aforementioned authors invoke processes of magmatic assimilation of sulfate, chloride, and carbonate salt from sedimentary rocks, which may trigger immiscible separation of iron-rich liquids in IOA systems. Even though the involvement of nontraditional ore fluids such as molten salts is plausible, the geologic and mineralogical characteristics observed at Vetas del Maule suggest that magnetite likely precipitated from hydrosaline liquids exsolved from a subvolcanic intrusion (Zhao et al., 2024). For example, hydrothermal alteration features are recognized within a zone that is distinguishable from adjacent unaltered units at 1:200,000 map scale (Hildreth et al., 2010; fig. 1 in Rojas et al., 2022) and include sinuous veins of tens of meters, some with large comb-textured crystals, pervasive albitization halos of several tens of meters, extensive hydrothermal breccias, and widespread magnetite disseminations. Further studies are required to confirm this hypothesis, constrain the precise nature of fluids, and determine the physicochemical conditions that led to IOA mineralization at Vetas del Maule.

Conclusions

This study documents a new occurrence of IOA-type mineralization hosted within andesites of the eroded La Zorra volcano in the Laguna del Maule Volcanic Complex, south-central Andes. Based on field observations and petrographic characterization, we identified five different mineralization types: (1) irregular bodies of massive magnetite, (2) pyroxene-actinolite-magnetite veins, (3) magnetite hydrothermal brec-

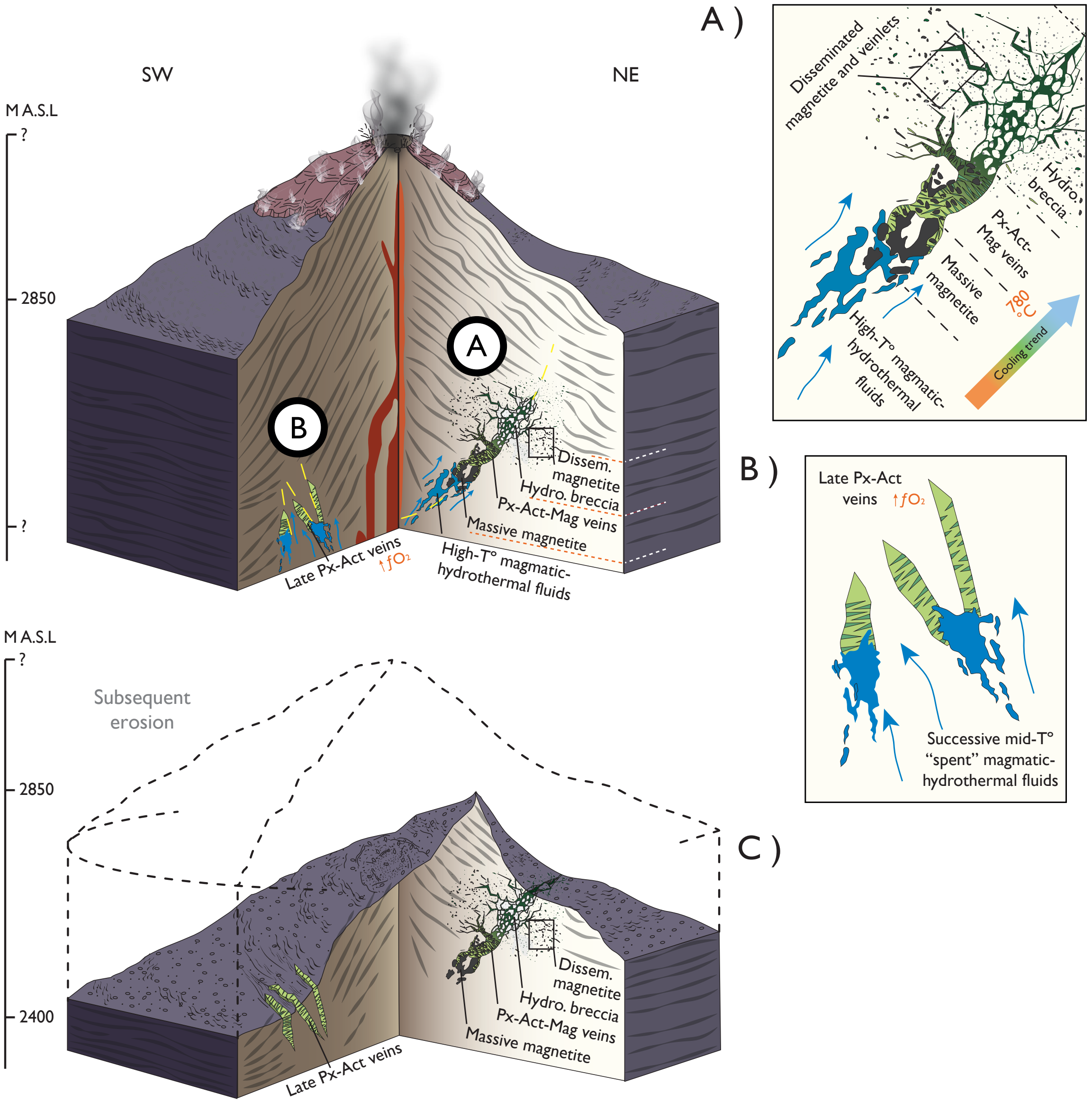

Fig. 10. Schematic genetic model for the Vetas del Maule system within the La Zorra volcano. (A) Progressive precipitation of magnetite follows the sequence as follows: massive magnetite, pyroxene-actinolite-magnetite veins, hydrothermal breccias, and disseminated magnetite by magmatic-hydrothermal fluids circulating through deep faults. (B) Subsequent formation of pyroxene-actinolite (± magnetite) veins in new zones of structural weakness, associated with lower temperature and more oxidized fluid(s). (C) Late glacial erosion and isostatic rebound exposes the different mineralization styles. Model not to scale; the size of the magnetite bodies has been exaggerated for better visualization. See text for discussion. Abbreviations: Act = actinolite, Dissem. = disseminated, High-T° = high-temperature, Hydro. = hydrothermal, Mag = magnetite, M A.S.L. = meters above sea level, Mid-T° = mid-temperature, Px = pyroxene.

cias, (4) disseminated magnetite, and (5) pyroxene-actinolite veins with minor magnetite. A wide diversity of magnetite microtextures were identified, including trellis-like oxyexsolutions, regular bands of microinclusions, overgrowths, and porous textures, many of which have been described in several IOA deposits worldwide.

EMPA analyses of magnetite show that the concentration of key elements—most notoriously Mg, Na, Si, and Mn and less evidently V, Ca, and potassium—vary as a function of mineralization style. In summary, EMPA data of the different types of magnetite reveal a dominant hydrothermal signature, with variable Fe concentrations and V/Ti ratios depending on the different styles of mineralization. Field observations, mineralogical examination, and microanalytical data suggest that most of the magnetite at Vetas del Maule formed from magmatically derived hydrothermal fluids.

Several microtextural and chemical characteristics of magnetite mineralization in Vetas del Maule are similar to those described in other Andean IOA deposits. The ^{40}Ar/^{39}Ar phlogopite age is interpreted as the time of magnetite mineralization (873.6 ± 30.3 ka plateau age), slightly younger than the andesite host rock (^{40}Ar/^{39}Ar plateau age of 1.013 ± 0.028 Ma, Hildreth et al., 2010), suggesting that the formation of the Vetas del Maule is closely related to the evolution of the La Zorra volcano-magmatic system. Therefore, we conclude that the IOA-type mineralization reported in this study was the result of processes that efficiently concentrated iron, probably via hydraulic injection of hydrosaline fluids with subsequent fracturing and decompression.

The study of this well-preserved, small, and therefore relatively simple IOA-type system can contribute to understanding several features of larger and more complex IOA deposits in the Andean province and elsewhere. Ultimately, Vetas del Maule presents evidence that IOA-type mineralization in modern volcanic arcs may be more common than previously thought, offering new opportunities for both research and exploration.

Acknowledgments

This work was funded by the National Research and Development Agency of Chile (ANID) through the Millennium Science Initiative Program (Millennium Nucleus for Metal Tracing Along Subduction, NCN13_065). Additional support was provided by ANID-Fondecyt grant 1190105, and National Science Foundation Earth Sciences (NSF EAR) 2233425, 2214119 (ACS). We thank Santiago Tassara, Gerd Sielfeld, Domínica Kausel, Diego Muñoz, and Ricardo Fuentealba for their assistance during field work. Irene del Real, Diego Morata, Francisco Delgado, Andrea Herazo, Rurik Romero, and María Rodriguez-Mustafa, are acknowledged for their helpful comments on an early version of this manuscript. We thank Editor-in-Chief Larry Meinert for handling of the manuscript and reviewers Lucas John Marshall, Matthew Steele-MacInniss, Martin Smith, and Patrick Krolop for their constructive assessment of this work.

REFERENCES

Andersen, N., Singer, B., Jicha, B., Fierstein, J., and Vazquez, J., 2013, The development of a restless rhyolite magma chamber at Laguna del Maule, Chile: AGU Fall Meeting Abstracts, San Francisco, California, 2013, V51C-2676.

Andersen, N., Singer, B., Jicha, B., Beard, B., Johnson, C., and Licciardi, J., 2017, Pleistocene to Holocene growth of a large upper crustal rhyolitic magma reservoir beneath the active Laguna del Maule volcanic field, central Chile: Journal of Petrology, v. 58, p. 85–114.

Bain, W.M., Steele-MacInnis, M., Li, K., Li, L., Mazdab, F.K., and Marsh, E.E., 2020, A fundamental role of carbonate-sulfate melts in the formation of iron oxide-apatite deposits: Nature Geoscience, v. 13, p. 751–757.

Bain, W.M., Steele-MacInnis, M., Tornos, F., Hanchar, J.M., Creaser, E.C., and Pietruszka, D.K., 2021, Evidence for iron-rich sulfate melt during magnetite(-apatite) mineralization at El Laco, Chile: Geology, v. 49, p. 1044–1048.

Barra, F., Reich, M., Selby, D., Rojas, P., Simon, A., Salazar, E., and Palma, G., 2017, Unraveling the origin of the Andean IOCG clan: A Re-Os isotope approach: Ore Geology Reviews, v. 81, p. 62–78.

Barton, M.D., 2014, Iron oxide (-Cu-Au-REE-P-Ag-U-Co) systems, *in* Holland, H.D., and Turkian, K.K., eds., Treatise on geochemistry, v. 13: Amsterdam, Elsevier, p. 515–541.

Barton, M.D., and Johnson, D.A., 2004, Footprints of Fe-oxide (-Cu-Au) systems: University of Western Australia, Special Publication 33, p. 112–116.

Borrok, D.M., Kelser, S.E., Boer, R.H., and Essene, E.J., 1998, The Vergenoeg magnetite-fluorite deposit, South Africa; support for a hydrothermal model for massive iron oxide deposits: Economic Geology, v. 93, v. 564–586.

Boutroy, E., Dare, S.S., Beaudoin, G., Barnes, S., and Lightfoot, P., 2014, Magnetite composition in Ni-Cu-PGE deposits worldwide: Application to mineral exploration: Journal of Geochemical Exploration, v. 145, p. 64–81.

Buddington, A.F., and Lindsley, D.H., 1964, Iron-titanium oxide minerals and synthetic equivalents: Journal of Petrology, v. 5, p. 310–357.

Canil, D., and Lacourse, T., 2020, Geothermometry using minor and trace elements in igneous and hydrothermal magnetite: Chemical Geology, v. 541, article 119576.

Cardona, C., Tassara, A., Gil-Cruz, F., Lara, L., Morales, S., Kohler, P., and Franco, L., 2018, Crustal seismicity associated to rapid surface uplift at Laguna del Maule Volcanic Complex, Southern volcanic zone of the Andes: Journal of Volcanology and Geothermal Research, v. 353, p. 83–94.

Childress, T., Simon, A., Day, W.C., Lundstrom, C.C., and Bindeman, I., 2016, Iron and oxygen isotope signatures of the Pea Ridge and Pilot Knob magnetite-apatite deposits, southeast Missouri, USA: Economic Geology, v. 111, p. 2033–2044.

Childress, T., Simon, A., Reich, M., Barra, F., Bilenker, L.D., La Cruz, N.L., Bindeman, I.N., and Ovalle, J.T., 2020, Triple oxygen ($\delta^{18}O$, $\Delta^{17}O$), hydrogen ($\delta^{2}H$), and iron ($\delta^{56}Fe$) stable isotope signatures indicate a silicate magma source and magmatic-hydrothermal genesis for magnetite orebodies at El Laco, Chile: Economic Geology, v. 115, p. 1519–1536.

Corona-Esquivel, R., Levresse, G., Solé, J., Henriquez, F., and Pi, T., 2018, New age in the geological evolution of the Cerro de Mercado iron oxide apatite deposit, Mexico: Implication in the Durango apatite standard (DAP) age variability: Journal of South American Earth Sciences, v. 88, p. 367–373.

Cox, S., Knackstedt, M., and Braun, J., 2001, Principles of structural control on permeability and fluid flow in hydrothermal systems: Reviews in Economic Geology, v.14, p. 1–24.

Dare, S.A., Barnes, S.J., and Beaudoin, G., 2015, Did the massive magnetite "lava flows" of El Laco (Chile) form by magmatic or hydrothermal processes? New constraints from magnetite composition by LA-ICP-MS: Mineralium Deposita, v. 50, p. 607–617.

Day, W.C., Slack, J.F., Ayuso, R.A., and Seeger, C.M., 2016, Regional geologic and petrologic framework for iron oxide ± apatite ± rare earth element and iron oxide copper-gold deposits of the Mesoproterozoic St. Francois Mountains terrane, southeast Missouri, USA: Economic Geology, v. 111, p. 1825–1858.

Deditius, A.P., Reich, M., Simon, A.C., Suvorova, A., Knipping, J., Roberts, M.P., and Saunders, M., 2018, Nanogeochemistry of hydrothermal magnetite: Contributions to Mineralogy and Petrology, v. 173, article 46, doi: 10.1007/s00410-018-1474-1.

Donovan, J.J., and Tingle, T.N., 1996, An improved mean atomic number background correction for quantitative microanalysis: Microscopy and Microanalysis, v. 2, p. 1–7.

Dupuis, C., and Beaudoin, G., 2011, Discriminant diagrams for iron oxide trace element fingerprinting of mineral deposit types: Mineralium Deposita, v. 46, p. 319–335.

Feigl, K.L., Le Mével, H., Tabrez Ali, S., Córdova, L., Andersen, N.L., DeMets, C., and Singer, B.S., 2014, Rapid uplift in Laguna del Maule volcanic field of the Andean Southern volcanic zone: Geophysical Journal International, v. 196, p. 885–901.

Fournier, T.J., Pritchard, M.E., and Riddick, S.N., 2010, Duration, magnitude, and frequency of subaerial volcano deformation events: New results from Latin America using InSAR and a global synthesis: Geochemistry, Geophysics, Geosystems, v. 11, article Q01003.

Gudmundsson, A., and Brenner, S., 2001, How hydrofractures become arrested: Terra Nova, v. 13, p. 456–462.

Hawkins, T., Smith, M.P., Herrington, R.J., Maslennikov, V., Boyce, A.J., Jeffries, T., and Creaser, R.A., 2017, The geology and genesis of the iron skarns of the Turgai belt, northwestern Kazakhstan: Ore Geology Reviews, v. 85, p. 216–246.

Heidarian, H., Lentz, D., Alirezaei, S., Peighambari, S., and Hall, D., 2016, Using the chemical analysis of magnetite to constrain various stages in the formation and genesis of the Kiruna-type Chadormalu magnetite-apatite deposit, Bafq district, Central Iran: Mineralogy and Petrology, v. 110, p. 927–942.

Hildreth, W., and Moorbath, S., 1988, Crustal contributions to arc magmatism in the Andes of central Chile: Contributions to Mineralogy and Petrology, v. 98, p. 455–489.

Hildreth, W., Godoy, E., Fierstein, J., and Singer, B., 2010, Laguna Del Maule volcanic field: Eruptive history of a Quaternary basalt-to-rhyolite distributed volcanic field on the Andean rangecrest in central Chile: Boletín del Servicio Nacional de Geología y Minería, v. 63, p. 1–145.

Hitzman, M.W., Oreskes, N., and Einaudi, M.T., 1992, Geological characteristics and tectonic setting of proterozoic iron oxide (Cu, U, Au, REE) deposits: Precambrian Research, v. 58, p. 241–287.

Hou, T., Charlier, B., Holtz, F., Veksler, I., Zhang, Z., Thomas, R., and Namur, O., 2018, Immiscible hydrous Fe-Ca-P melt and the origin of iron oxide-apatite ore deposits: Nature Communications, v. 9, p. 1–8.

Hu, B., Zeng, L.P., Liao, W., Wen, G., Hu, H., Li, M.Y.H., and Zhao, X., 2022, The origin and discrimination of high-Ti magnetite in magmatic-hydrothermal systems: Insight from machine learning analysis: Economic Geology, v. 117, p. 1613–1627.

Hu, H., Lentz, D., Li, J., McCarron, T., Zhao, X., and Hall, D., 2015, Reequilibration processes in magnetite from iron skarn deposits: Economic Geology, v. 110, p. 1–8.

Huang, X.W., and Beaudoin, G., 2019, Textures and chemical compositions of magnetite from iron oxide copper-gold (IOCG) and Kiruna-type iron oxide-apatite (IOA) deposits and their implications for ore genesis and magnetite classification schemes: Economic Geology, v. 114, p. 953–979.

——2021, Nanoinclusions in zoned magnetite from the Sossego IOCG deposit, Carajás, Brazil: Implication for mineral zoning and magnetite origin discrimination: Ore Geology Reviews, v. 139, article 104453.

Jicha, B., Singer, B.S., and Sobol, P., 2016, Re-evaluation of the ages of ^{40}Ar/^{39}Ar sanidine standards and supereruptions in the western US using a Noblesse multi-collector mass spectrometer: Chemical Geology, v. 431, p. 54–66.

Jonsson, E., Troll, V., Högdahl, K., Harris, C., Weis, F., Nilsson, K.P., and Skelton, A., 2013, Magmatic origin of giant “Kiruna-type” apatite-iron-oxide ores in central Sweden: Scientific Reports, v. 3, article 1644.

Keller, T., Tornos, F., Hanchar, J.M., Pietruszka, D.K., Soldat, A., Dingwell, D.B., and Suckale, J., 2022, Genetic model of the El Laco magnetite-apatite deposits by extrusion of iron-rich melt: Nature Communications, v. 13, article 6114.

Knipping, J.L., Bilenker, L.D., Simon, A.C., Reich, M., Barra, F., Deditius, A.P., and Munizaga, R., 2015a, Giant Kiruna-type deposits form by efficient flotation of magmatic magnetite suspensions: Geology, v. 43, p. 591–594.

Knipping, J.L., Bilenker, L.D., Simon, A.C., Reich, M., Barra, F., Deditius, A.P., and Munizaga, R., 2015b, Trace elements in magnetite from massive iron oxide-apatite deposits indicate a combined formation by igneous and magmatic-hydrothermal processes: Geochimica et Cosmochimica Acta, v. 171, p. 15–38.

Kohn, M.J., 2017, Titanite petrochronology: Reviews in Mineralogy and Geochemistry, v. 83, p. 419–441.

La Cruz, N.L., Ovalle, J.T., Simon, A.C., Konecke, B.A., Barra, F., Reich, M., Leisen, M., and Childress, T.M., 2020, The geochemistry of magnetite and apatite from the El Laco iron oxide-apatite deposit, Chile: Implications for ore genesis: Economic Geology, v. 115, p. 1461–1491.

Le Mével, H., Gregg, P.M., and Feigl, K.L., 2016, Magma injection into a long-lived reservoir to explain geodetically measured uplift: Application to the 2007–2014 unrest episode at Laguna del Maule volcanic field, Chile: Journal of Geophysical Research: Solid Earth, v. 121, p. 6092–6108.

Lledo, H.L., and Jenkins, D.M., 2008, Experimental investigation of the upper thermal stability of Mg-rich actinolite; implications for Kiruna-type iron deposits: Journal of Petrology, v. 49, p. 225–238.

Makvandi, S., Ghasemzadeh-Barvarz, M., Beaudoin, G., Grunsky, E.C., McClenaghan, M.B., and Duchesne, C., 2016, Principal component analysis of magnetite composition from volcanogenic massive sulfide deposits: Case studies from the Izok Lake (Nunavut, Canada) and Halfmile Lake (New Brunswick, Canada) deposits: Ore Geology Reviews, v. 72, p. 60–85.

Manconi, A., Longpré, M., Walter, T., Troll, V., and Hansteen, T., 2009, The effects of flank collapses on volcano plumbing systems: Geology, v. 37, p. 1099–1102.

McCurdy, M., Peter, J., McClenaghan, M., Gadd, M., Layton-Matthews, D., Leybourne, M., Garrett, R., Petts, D., Jackson, S., and Casselman, S., 2022, Evaluation of magnetite as an indicator mineral for porphyry Cu exploration: A case study using bedrock and stream sediments at the Casino porphyry Cu-Au-Mo deposit, Yukon, Canada: Geochemistry: Exploration, Environment, Analysis, v. 22, article geochem2021-072.

Min, K., Mundil, R., Renne, P., and Ludwig, K., 2000, A test for systematic errors in ^{40}Ar/^{39}Ar geochronology through comparison with U/Pb analysis of a 1.1-Ga rhyolite: Geochimica et Cosmochimica Acta, v. 64, p. 73–98.

Mumin, A., Corriveau, L., Somarin, A., and Ootes, L., 2007, Iron oxide copper-gold-type polymetallic mineralization in the Contact Lake belt, Great Bear magmatic zone, Northwest Territories, Canada: Exploration and Mining Geology, v. 16, p. 187–208.

Mungall, J.E., Long, K., Brenan, J.M., Smythe, D., and Naslund, H.R., 2018, Immiscible shoshonitic and Fe-P-oxide melts preserved in unconsolidated tephra at El Laco volcano, Chile: Geology, v. 46, p. 255–258.

Nadoll, P., Angerer, T., Mauk, J.L., French, D., and Walshe, J., 2014, The chemistry of hydrothermal magnetite: A review: Ore Geology Reviews, v. 61, p. 1–32.

Naranjo, J.A., Henríquez, F., and Nyström, J.O., 2010, Subvolcanic contact metasomatism at El Laco volcanic complex, central Andes: Andean Geology, v. 37, p. 110–120.

Naslund, H.R., Henríquez, F., Nyström, J.O., Vivallo, W., and Dobbs, F.M., 2002, Magmatic iron ores and associated mineralization: Examples from the Chilean high Andes and coastal Cordillera, *in* Porter, T.M., ed., Hydrothermal iron oxide copper gold and related deposits: A global perspective, v. 2: Adelaide, PGC Publishing, p. 207–226.

Norton, D.L., and Cathles, L.M., 1973, Breccia pipes, products of exsolved vapor from magmas: Economic Geology, v. 68, p. 540–546.

Novoa, C., Rémy, D., Gerbault, M., Baez, J., Tassara, A., Cordova, L., Cardona, C., Granger, M., Bonvalot, F., and Delgado, F., 2019, Viscoelastic relaxation: A mechanism to explain the decennial large surface displacements at the Laguna del Maule silicic volcanic complex: Earth and Planetary Science Letters, v. 521, p. 46–59.

Nyström, J.O., and Henriquez, F., 1994, Magmatic features of iron ores of the Kiruna type in Chile and Sweden; ore textures and magnetite geochemistry: Economic Geology, v. 89, p. 820–839.

Olivares, V., Cembrano, J., Arancibia, G., Reyes, N., Herrera, V., and Faulkner, D., 2010, Significado tectónico y migración de fluidos hidrotermales en una red de fallas y vetas de un Dúplex de rumbo: Un ejemplo del Sistema de Falla de Atacama: Andean Geology, v. 37, p. 473–497.

Ovalle, J.T., La Cruz, N.L., Reich, M., Barra, F., Simon, A.C., Konecke, B.A., Rodriguez-Mustafa, M., Deditius, A., Childress, T., and Morata, D., 2018, Formation of massive iron deposits linked to explosive volcanic eruptions: Scientific Reports, v. 8, p. 1–11.

Ovalle, J.T., Reich, M., Barra, F., Simon, A.C., Deditius, A.P., Le Vaillant, M., Neill, O.K., Palma, G., Romero, R., Román, N., La Cruz, N.L., Roberts, M.P., and Morata, D., 2022, Magmatic-hydrothermal evolution of the El Laco iron deposit revealed by trace element geochemistry and high-resolution chemical mapping of magnetite assemblages: Geochimica et Cosmochimica Acta, v. 330, 230–257.

Ovalle, J.T., Reich, M., Barra, F., Simon, A.C., Godel, B., Le Vaillant, M., Palma, G., Deditius, A., Heuser, G., Arancibia, G., and Morata, D., 2023, Fluid-assisted aggregation and assembly of magnetite microparticles in the giant El Laco iron oxide deposit, Central Andes: ACS Earth and Space Chemistry, v. 7, 1378–1387.

Palma, G., Barra, F., Reich, M., Valencia, V., Simon, A., Vervoort, J., and Romero, R., 2019, Halogens, trace element concentrations, and Sr-Nd isotopes in apatite from iron oxide-apatite (IOA) deposits in the Chilean iron belt: Evidence for magmatic and hydrothermal stages of mineralization: Geochimica et Cosmochimica Acta, v. 246, p. 515–540.

Palma, G., Barra, F., Reich, M., Simon, A., and Romero, R., 2020, A review of magnetite geochemistry of Chilean iron oxide-apatite (IOA) deposits and its implications for ore-forming processes: Ore Geology Reviews, v. 126, article 103748.

Palma, G., Reich, M., Barra, F., Ovalle, J.T., Real, I., and Simon, A., 2021, Thermal evolution of Andean iron oxide-apatite (IOA) deposits as revealed by magnetite thermometry: Scientific Reports, v. 11, article 18424.

Pardo-Casas, F., and Molnar, P., 1987, Relative motion of the Nazca (Farallon) and South American plates since Late Cretaceous time: Tectonics, v. 6, p. 233–248.

Parente, C.V., Vieira Veríssimo, C.U., Francisquini, N., Perez Xavier, R., Menez, J., de Oliveira, R., Araújo da Silva, C.D., and Saraiva dos Santos, T.J., 2019, Geology, petrography and mineral chemistry of iron oxide-apatite occurrences (IOA type), western sector of the Neoproterozoic Santa Quiteria magmatic arc, Ceará northeast, Brazil: Ore Geology Reviews, v. 112, article 103024.

Peters, S.T., Alibabaie, N., Pack, A., McKibbin, S.J., Raeisi, D., Nayebi, N., Torab, F., Ireland, T., and Lehmann, B., 2019, Triple oxygen isotope variations in magnetite from iron-oxide deposits, central Iran, record magmatic fluid interaction with evaporite and carbonate host rocks: Geology, v. 48, p. 211–215.

Putnis, A., 2009, Mineral replacement reactions: Reviews in Mineralogy and Geochemistry, v. 70, p. 87–124.

——2015, Transient porosity resulting from fluid-mineral interaction and its consequences: Reviews in Mineralogy and Geochemistry, v. 80, p. 1–23.

Reich, M., Simon, A.C., Barra, F., Palma, G., Hou, T., and Bilenker, L.D., 2022, Formation of iron oxide-apatite deposits: Nature Reviews Earth and Environment, v. 3, p. 758–775, doi: 10.1038/s43017-022-00335-3.

Rhodes, A.L., and Oreskes, N., 1999, Oxygen isotope composition of magnetite deposits at El Laco, Chile: Evidence of formation from isotopically heavy fluids: Society of Economic Geologists, Special Publication 7, p. 333–351.

Rodriguez-Mustafa, M.A., Simon, A.C., del Real, I., Thompson, J.F.H., Bilenker, L.D., Barra, F., Bindeman, I., and Cadwell, D., 2020, A continuum from iron oxide copper-gold to iron oxide-apatite deposits: Evidence from Fe and O stable isotopes and trace element chemistry of magnetite: Economic Geology, v. 115, p. 1443–1459.

Rojas, P., Barra, F., Deditius, A., Reich, M., Simon, A., Roberts, M., and Rojo, M., 2018, New contributions to the understanding of Kiruna-type iron oxide-apatite deposits revealed by magnetite ore and gangue mineral geochemistry at the El Romeral deposit: Ore Geology Reviews, v. 93, p. 413–435.

Rojas A, Sruoga, P., Lamberti, M., Agusto, M., Tondreau, J., Mendoza, N., Daniele, L., and Morata, D., 2022, Unravelling the hydrothermal system of Laguna del Maule restless volcanic field, in the Andean Southern volcanic zone (36° 10′ S): Journal of Volcanology and Geothermal Research, v. 424, article 107498.

Ross, J., 2019, Data acquisition and processing framework for Ar-Ar geochronology and noble gas mass spectrometry: doi: 10.5281/zenodo.3237834.

Salazar, E., Barra, F., Reich, M., Simon, A., Leisen, M., Palma, G., and Rojo, M., 2020, Trace element geochemistry of magnetite from the Cerro Negro Norte iron oxide-apatite deposit, northern Chile: Mineralium Deposita, v. 55, p. 409–428.

Sibson, R., 2001, Seismogenic framework for hydrothermal transport and ore deposition: Reviews in Economic Geology, v. 14, p. 25–50.

Sillitoe, R., 2003, Iron oxide-copper-gold deposits: An Andean view: Mineralium Deposita, v. 38, p. 787–812.

Sillitoe, R., and Burrows, D., 2002, New field evidence bearing on the origin of the El Laco magnetite deposit, northern Chile: Economic Geology, v. 97, p. 1101–1109.

Simon, A.C., Pettke, T., Candela, P.A., Piccoli, P.M., and Heinrich, C.A., 2004, Magnetite solubility and iron transport in magmatic-hydrothermal environments: Geochimica et Cosmochimica Acta, v. 68, p. 4905–4914.

Simon, A.C., Kniping, J., Reich, M., Barra, F., Deditius, A.P., Bilenker, L., and Childress, T., 2018, Kiruna-type iron oxide- apatite (IOA) and iron oxide copper-gold (IOCG) deposits form by a combination of igneous and magmatic-hydrothermal processes: Evidence from the Chilean iron belt: Society of Economic Geologists, Special Publication 21, p. 89–114.

Singer, B., Hildreth, W., and Vincze, Y., 2000, ^{40}Ar/^{39}Ar evidence for early deglaciation of the central Chilean Andes: Geophysical Research Letters, v. 27, p. 1663–1666.

Singer, B., Andersen, N.L., Le Mével, H., Feigl, K.L., DeMets, C., Tikoff, B., Thurber, C.H., Jicha, B., Cardona, C., Córdova, L., et al., 2014, Dynamics of a large, restless, rhyolitic magma system at Laguna del Maule, southern Andes, Chile: GSA Today, v. 24, p. 4–10.

Singer, B., Le Mével, H., Licciardi, M., Córdova, L., Tikoff, B., Garibaldi, N., Andersen, N., Diefenbach, A., and Feigl, K., 2018, Geomorphic expression of rapid Holocene silicic magma reservoir growth beneath Laguna del Maule, Chile: Science Advances, v. 4, article eaat1513.

Sullivan, B., Locmelis, M., Tunnell, B.N., Seeger, C., Moroni, M., Dare, S., Ryan M., and Schott, T., 2023, Genesis of the 1.45 Ga Kratz Spring iron oxide-apatite deposit complex in southeast Missouri, USA: Constraints from oxide mineral chemistry: Economic Geology, v. 118, p. 1149–1175.

Tan, W., Liu, P., He, H., Wang, C.Y., and Liang, X., 2016, Mineralogy and origin of exsolution in Ti-rich magnetite from different magmatic Fe-Ti oxide-bearing intrusions: The Canadian Mineralogist, v. 54, p. 539–553.

Taylor, R.D., Shah, A.K., Walsh, G.J., and Taylor, C.D., 2019, Geochemistry and geophysics of iron oxide-apatite deposits and associated waste piles with implications for potential rare earth element resources from ore and historical mine waste in the eastern Adirondack Highlands, New York, USA: Economic Geology, v. 114, p. 1569–1598.

Tornos, F., Velasco, F., and Hanchar, J.M., 2016, Iron-rich melts, magmatic magnetite, and superheathed hydrothermal systems: The El Laco deposit, Chile: Geology, v. 44, p. 427–430.

Tornos, F., Hanchar, J.M., Steele-MacInnis, M., Crespo, E., Kamenetsky, V., and Casquet, C., 2024, Formation of magnetite-(apatite) systems by crystallizing ultrabasic iron-rich melts and slag separation: Mineralium Deposita, v. 59, p. 189–225.

Troll, V.R., Weis, F.A., Jonsson, E., Andersson, U.B., Majidi, S.A., Högdahl, K., Harris, C., Millet, M.A., Saravanan Chinnasamy, S., Koojiman, E., and Nilsson, K.P., 2019, Global Fe-O isotope correlation reveals magmatic origin of Kiruna-type apatite-iron-oxide ores: Nature Communications, v. 10, p. 1–12.

Vargas R.R., Gustafson, L.B., Vukasovic, M., Tidy F.E., and Skewes, M.A., 1999, Ore breccias in the Rio Blanco-Los Bronces porphyry copper deposit, Chile: Society of Economic Geologists, Special Publication 7, p. 281–297.

Velasco, F., Tornos, F., and Hanchar, J.M., 2016, Immiscible iron- and silica-rich melts and magnetite geochemistry at the El Laco volcano (northern Chile): Evidence for a magmatic origin for the magnetite deposits: Ore Geology Reviews, v. 79, p. 346–366.

Verdugo-Ihl, M., Ciobanu, C., Cook, N., Ehrig, K., Slattery, A., Courtney-Davies, L., and Dmitrijeva, M., 2021, Nanomineralogy of hydrothermal magnetite from Acropolis, South Australia: Genetic implications for iron-oxide copper gold mineralization: American Mineralogist, v. 106, p. 1273–1293.

Wang, Y., Zhu, W., Huang, H., Bai, Z., Zhong, H., Yao, J., and Fan, H., 2020, Geochemistry of magnetite from the giant Paleoproterozoic Dahongshan Fe-Cu deposit, SW China: Constraints on nature of ore-forming fluids and depositional setting: Ore Geology Reviews, v. 118, article 103361.

Wen, G., Li, J. W., Hofstra, A.H., Koening, A.E., Lowers, H.A., and Adams, D., 2017, Hydrothermal reequilibration of igneous magnetite in altered granitic plutons and its implications for magnetite classification schemes: Insights from the Handan-Xingtai iron district, North China craton: Geochimica et Cosmochimica Acta, v. 213, p. 255–270.

Wespestad, C.E., Thurber, C.H., Andersen, N.L., Singer, B.S., Cardona, C., Zeng, X., Bennington, N.L., Keranen, K., Peterson, D.E., Cordell, D., et al., 2019, Magma reservoir below Laguna del Maule volcanic field, Chile, imaged with surface-wave tomography: Journal of Geophysical, v. 124, p. 2858–2872.

Westhues, A., Hanchar, J.M., LeMessurier, M.J., and Whitehouse, M.J., 2017a, Evidence for hydrothermal alteration and source regions for the Kiruna iron oxide-apatite ore (northern Sweden) from zircon Hf and O isotopes: Geology, v. 45, p. 571–574.

Westhues, A., Hanchar, J.M., Voisey, C.R., Whitehouse, M.J., Rossman, G.R., and Wirth, R., 2017b, Tracing the fluid evolution of the Kiruna iron oxide apatite deposits using zircon, monazite, and whole rock trace elements and isotopic studies: Chemical Geology, v. 466, p. 303–322.

Williams, P.J., Barton, M.D., Johnson, D.A., Fontboté, L., De Haller, A., Mark, G., and Marschik, R., 2005, Iron oxide copper-gold deposits: Geology, space-time distribution, and possible modes of origin: Economic Geology 100th Anniversary Volume, p. 371–405.

Xirouchakis, D., Lindsley, D.H., and Frost, B.R., 2001a, Ca-Mg-Fe olivine and pyroxenes, Fe-Mg-Ti oxides, and quartz: Part I. Theory: American Mineralogist, v. 86, p. 247–253.

——2001b, Assemblages with titanite ($CaTiOSiO_4$), Ca-Mg-Fe olivine and pyroxenes, Fe-Mg-Ti oxides, and quartz: Part II. Application: American Mineralogist,v. 86, p. 254–264.

Xu, X., Bain, W.M., Tornos, F., Hanchar, J.M., Lamadrid, H.M., Lehmann, B., Xiaochun, X., Steadman, J.A., Bottrill, R.S., Soleymani, M., et al., 2024, Magnetite-apatite ores record widespread involvement of molten salts: Geology, doi: 10.1130/G51887.1.

Ye, Z., Mao, J., Yang, C., Usca, J., and Li, X., 2023, Trace elements in magnetite and origin of the Mariela iron oxide-apatite deposit, southern Peru: Minerals, v. 13, article 934.

Yin, S., Wirth, R., Ma, C., and Xu, J., 2019, The role of mineral nanoparticles at a fluid-magnetite interface: Implications for trace-element uptake in hydrothermal systems: American Mineralogist, v. 104, p. 1180–1188.

Zhao, X., Zeng, L.P., Liao, W., Fan, Y.Z., Hofstra, A.H., Emsbo, P., Hu, H., Wen, G., and Li, J.W., 2024, Iron oxide-apatite deposits form from hydrosaline liquids exsolved from subvolcanic intrusions: Mineralium Deposita, v. 59, p. 655–669.

Ernesto Cofré Arzola is an exploration geologist with a track record in major mining companies like Newcrest Mining and Fortescue Metals Chile. He earned his B.Sc. in geology from the University of Concepción (2018) and his M.Sc. in geology from the University of Chile (2022). During his M.Sc., he conducted research at the Millennium Nucleus for Metal Tracing Along Subduction (Science Government Initiative Program NCN13_065) specializing in the formation mechanisms and characterization of iron oxide-apatite (IOA) and iron oxide copper-gold deposits.